

# Salient Object Detection in Complex Weather Conditions via Noise Indicators

Quan Chen, Xiaokai Yang, Tingyu Wang, Rongfeng Lu, Xichun Sheng, Yaoqi Sun, Chenggang Yan

**Abstract**—Salient object detection (SOD), a foundational task in computer vision, has advanced from single-modal to multi-modal paradigms to enhance generalization. However, most existing SOD methods assume low-noise visual conditions, overlooking the degradation of segmentation accuracy caused by weather-induced noise in real-world scenarios. In this paper, we propose a SOD framework tailored for diverse weather conditions, encompassing a specific encoder and a replaceable decoder. To enable handling of varying weather noises, we introduce a one-hot vector as a noise indicator to represent different weather types and design a Noise Indicator Fusion Module (NIFM). The NIFM takes both semantic features and the noise indicator as dual inputs and is inserted between consecutive stages of the encoder to embed weather-aware priors via adaptive feature modulation. Critically, the proposed specific encoder retains compatibility with mainstream SOD decoders. Extensive experiments are conducted on the WXSOD dataset under varying training data scales (100%, 50%, 30% of the full training set), three encoder and seven decoder configurations. Results show that the proposed SOD framework (particularly the NIFM-enhanced specific encoder) improves segmentation accuracy under complex weather conditions compared to a vanilla encoder.

**Index Terms**—Salient object detection, weather noise, noise indicator, encoder

## I. INTRODUCTION

**S**ALIENT object detection (SOD), a fundamental task in computer vision, aims to mimic the attention mechanism of the human visual system to accurately locate and highlight the most visually attractive regions in complex scenes. As a core technology supporting downstream applications, SOD has long remained a research focus. With the advancement of studies, this field has achieved a leap from single-modality RGB SOD [1]–[6] to multi-modality paradigms, including RGB-Thermal [7]–[9], RGB-Depth [10]–[12], even triple-modal RGB-Depth-Thermal SOD [13]–[15]. These advancements enhance the generalization ability and scene adaptability of SOD models.

Quan Chen is with the School of Automation, Hangzhou Dianzi University, Hangzhou 310018, China, and also with the College of Artificial Intelligence, Jiaxing University, Jiaxing 314001, China (e-mail:chenquan@aluhdu.edu.cn).

Xiaokai Yang and Tingyu Wang are with the School of Communication Engineering, Hangzhou Dianzi University, Hangzhou 310018, China (e-mail:242080082@hdu.edu.cn, tingyu.wang@hdu.edu.cn).

Rongfeng Lu and Chenggang Yan are with the School of Automation, Hangzhou Dianzi University, Hangzhou 310018, China (e-mail:rongfenglu@hdu.edu.cn, cgyan@hdu.edu.cn).

Xichun Sheng is with the School of Faculty of Applied Science, Macao Polytechnic University, Macao, China (email:p2314922@mpu.edu.mo)

Yaoqi Sun is with the School of Mathematics and Computer Science, Lishui University, Lishui 323000, and also with the Lishui Institute of Hangzhou Dianzi University, Lishui 323050, China (email:sunyq2233@163.com)

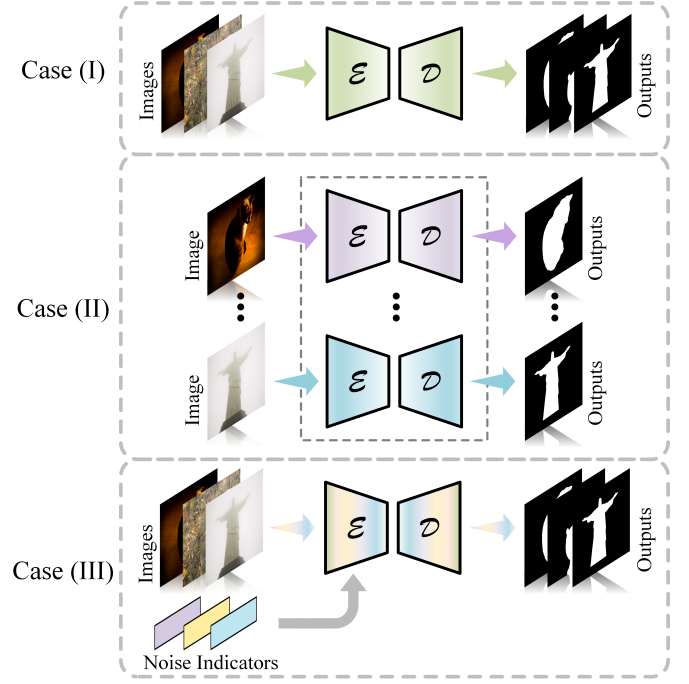


Fig. 1. Three paradigms for salient object detection under complex weather conditions. Case (I): A unified network is used for both training and testing, without accounting for the variations in weather-induced noise. Case (II): A distinct model is trained independently for images with different weather noise, incurring significant computational redundancy. Case (III): Our proposed framework, which introduces a noise indicator to highlight the differences between various weather noises, thereby enhancing the network's detection robustness across diverse weather conditions.

Despite these notable advances, most existing SOD methods assume that input images are under ideal visual conditions (*i.e.*, noise-free or low-noise environments), ignoring the impact of weather-induced noise on segmentation accuracy in real-world scenarios. With the rapid expansion of computer vision into practical applications, research focus has shifted toward algorithm design for low-quality scenarios, a trend that has further prompted the development of unified models to enhance robustness under diverse weather conditions. For instance, in tasks such as image restoration [16]–[18] and retrieval [19]–[21], several studies have built unified frameworks to mitigate weather-related distortions. These efforts motivate us to develop a SOD framework capable of handling complex weather-corrupted inputs while maintaining compatibility with prevailing SOD methods.

We first analyzes two typical strategies to process diverse weather-corrupted images, alongside the proposed general

strategy, as illustrated in Fig. 1. Case (I): Images with various weather noises are utilized for training and testing without differentiation. This strategy entirely neglects the inherent variations between different weather noises types, resulting to constrained model adaptability in complex conditions. Case (II): A specialized model is trained for each weather type. Although tailored to specific noise patterns, it requires storing multiple sets of model parameters, inevitably increasing computational costs. Case (III): The proposed general strategy guides the encoder to learn discriminative feature representations related to noise via noise indicators, while ensuring compatibility with a wide range of existing decoders. Compared with the first two cases, our strategy combines the advantages of both: it employs a single encoder for architectural simplicity, yet enhances discriminative capability across weather types through explicit noise-aware conditioning.

To implement this general strategy, we decompose the SOD framework into core components: a specific encoder and a replaceable decoder, with our design efforts focused on the specific encoder. Specifically, we introduce a one-hot vector to represent distinct weather noise types, and propose a Noise Indicator Fusion Module (NIFM) that accepts both semantic features and the one-hot vector as dual inputs. NIFM is inserted between consecutive stages of the backbone network to progressively embed weather priors, thereby guiding the encoder to learn unified and robust multi-scale semantic features through adaptive feature modulation. Crucially, the specific encoder retains compatibility with mainstream SOD decoders, enabling direct integration into existing SOD pipelines without requiring structural adjustments. Experimental results on the WXSOD dataset show that the proposed SOD framework improve segmentation accuracy under complex weather conditions across varying training data scales, backbone and decoder architectures, providing a feasible pathway toward diverse-weather SOD. Our primary contributions are summarized as follows:

- We propose a SOD framework tailored to diverse weather conditions, comprising a specific encoder and a replaceable decoder.
- We design a NIFM taking semantic features and a noise indicator as dual inputs and guiding the encoder to learn robust feature representations
- Experiments results on the WXSOD dataset, as well as under different backbone and decoder configurations, have verified the effectiveness of our method.

The rest of the paper is organized as follows: Section II presents related work, focusing on single-modality and multi-modality SOD. In Section III, we detail our proposed method, including the method overview and each component. Section IV presents our experimental results, and Section V provides concluding remarks.

## II. RELATED WORK

### A. RGB SOD

Salient Object Detection has garnered significant research interest in recent years, leading to the proposal of numerous

SOD methods. Traditional methods [22], [23] primarily relied on handcrafted low-level visual features, such as color contrast, edge information, and texture consistency. Although these models perform adequately in simple backgrounds, they are susceptible to interference and exhibit poor robustness when confronted with complex scenes.

In contrast, convolutional neural networks (CNN) have achieved remarkable success in a wide range of computer vision tasks [24]–[35]. Researchers have proposed numerous CNN-based SOD models, which are underpinned by diverse theoretical paradigms such as visual attention mechanisms [36], the interaction of multi-level features [37] and the utilization of edge information [38]. These innovations have considerably advanced SOD performance. However, current SOD datasets [39]–[43] neglect noise interference, resulting in learning-based methods being sensitive to noise. To address this gap, Wan *et al.* [44] introduced salt-and-pepper noise with varying intensities to guide models in learning noise-robust feature representations. To mitigate the effects of image dark degradation and low contrast, Yu *et al.* [45] combined SOD networks with low-light enhancement techniques to form a novel learning framework, while constructing the first dedicated SOD dataset for low-light scenarios. These datasets suffer from limited noise diversity and fail to real-world complexity. Consequently, Yuan *et al.* [46] made a preliminary attempt to incorporate weather noise into ORSI SOD, adding fog and rain noise to enhance the generalization of the model, but did not construct a benchmark. Chen *et al.* [47] developed the WXSOD, the first large-scale SOD dataset incorporating both diverse synthetic and real-world noises under adverse weather conditions. Differ from specific-structured models, our objective is to develop a simple yet effective framework capable of enhancing the saliency detection accuracy of various methods under extreme weather conditions.

### B. Multi-modal SOD

As complementary information to RGB images, depth and thermal modalities have been widely adopted in SOD tasks. These complementary properties have spurred rapid advancements in multi-modality SOD, leading to specialized sub-tasks, including RGB-D SOD, RGB-T SOD, and RGB-DT SOD.

In the RGB-D SOD domain, research focuses on exploring correlations and disparities between RGB and depth features [48]–[53]. For instance, Piao *et al.* [54] introduced a depth distiller to transfer depth knowledge from the depth stream to the RGB stream, eliminating redundant depth information. To mitigate this limitation, recent studies emphasize optimized feature fusion strategies, which can be divided into two categories: i) Pixel-level fusion: This approach concatenates RGB and depth images into four-channel inputs processed by a single-stream network. ii) Feature-level fusion: As the predominant paradigm in current RGB-D SOD research, this strategy extracts uni-modal features via dual-branch networks before integration. For instance, Liu *et al.* [55] enhanced cross-modal interactions through mutual attention combined with contrast learning and adaptive selective attention. In the parallel field of RGB-T SOD, Tu *et al.* [56] planned a large-scale RGB-T dataset with degraded samples and developed an

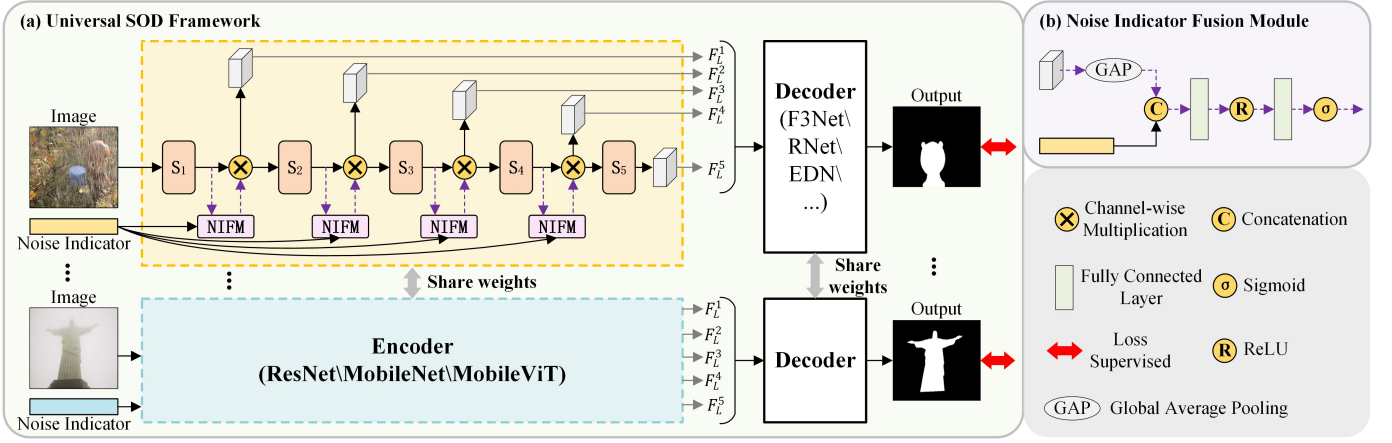


Fig. 2. The diagram of the proposed framework. The input image and noise indicator are first fed into the specific encoder to extract multi-scale semantic features. Then, the replaceable decoder is adopted to map semantic features into salient images. Note that we employ 7 various decoders to verify the feasibility of the proposed framework.

end-to-end network for adaptive salient cue selection. From the perspective of network structure optimization, it is worth noting that the technical advancements developed for RGB-D SOD models and RGB-T SOD models exhibit significant interconnections [9], [57]–[62]. To transcend dual-modality constraints, RGB-DT SOD integrates three modalities to enhance saliency detection accuracy in complex scenarios [13]–[15], [63], [64]. Toward enhanced deployment flexibility, recent advances leverage [65]–[67] leverage modality-type indicators or prompt learning to construct SOD frameworks compatible with different modality inputs. For instance, Huang *et al.* [65] incorporated one-hot encoding of image modality types into the model architecture, thereby enhancing the accuracy and generalization of multi-modal SOD. Inspired by these developments, we posit that explicitly distinguishing noise types of RGB images captured under diverse weather conditions is promising to enhance SOD robustness against varying noise interference. Based on this insight, this paper introduces a novel noise-prompted SOD framework designed for complex weather conditions.

### C. Object detection in Adverse Weather Conditions

Recent studies on object detection have focused on improving detection accuracy under adverse weather conditions. These methods can be classified into three categories according to their implementation workflows. The first category [68] directly trains models on images captured under real or simulated adverse weather. Although this strategy improves model performance in complex conditions, it requires constructing datasets covering diverse adverse weather scenarios. The second category [69] employs a two-stage workflow that first applies image restoration methods [70] to denoise images and then feeds the restored images into object detection models for detection. While these methods improve image clarity, their performance generally lags behind the first category, largely because image restoration process may alter-intrinsic the original features of images. The third category [71] integrates weather-aware image enhancement

techniques into the detection framework or utilizes domain adaptation to minimize the domain shift between clear-weather training data and adverse-weather test data. Although these approaches often surpass the second category in performance, studies [72], [73] indicate that their detection results are less consistent than those achieved by models trained directly on adverse weather images. Inspired by the aforementioned works, we propose a novel framework to achieve salient object detection in complex weather scenarios.

## III. METHODOLOGY

In this section, we detail the proposed network. In Section III-A, we give an overview of the basic network architecture. In Section III-B, we present the Noise Indicator Fusion Module in detail. After that, in Section III-C, we have provided details of various decoders. Finally, in Section III-D, we further discuss the basic network framework.

### A. Overview

The overview of our framework is shown in Fig. 2. Given an input image  $I_{in} \in \mathbb{R}^{H \times W \times C}$  with a known noise type, we first construct a noise indicator  $T \in \mathbb{R}^M$  that uniquely encodes the noise type. This one-hot representation corresponds to  $M$  predefined weather-induced noise categories. Both  $I_{in}$  and  $T$  are then fed into a ResNet-50 backbone to extract multi-scale semantic features  $\{F_i\}_{i=1}^5$ . To enable interaction between noise indicator and semantic features, a Noise Indicator Fusion Module (NIFM) is inserted between every two consecutive stages of ResNet-50. Then, a replaceable decoder is employed to map the multi-scale semantic features into a saliency map. It is worth noting that we focus on designing a general framework rather than a specific network structure. Therefore, we implement our framework with 7 various decoders (including F3Net [74], R-Net [75], MINET [37], AESINet [76], BAFSNet [77], DC-Net [78] and EDN [79]) for comprehensive validation. Decoder implementations follow original configurations as described in the cited publications.

### B. Noise-indicator Fusion Module

Studies addressing weather noise variations in other visual tasks often attempt to explicitly incorporate weather-type encoding vectors [80], [81] or insert learnable vectors [82], [83], thereby guiding networks to distinguish differences in image noise. Meanwhile, emerging studies [65]–[67] in SOD focus on designing multi-modal unified frameworks, employing similar approaches to empower the model to discern and adapt to different input data modalities. Inspired by these efforts, we design a Noise Indicator Fusion Module including a noise indicator. Assuming there are  $M$  types of weather-noise, the noise indicator  $T \in \mathbb{R}^M$  is a one-hot encoded vector of length  $M$ , where the element corresponding to the noise type of the input image is set to 1, and other elements are set to 0. For instance, the noise indicator for rain images is  $[0, 1, 0, 0, 0, 0, 0, 0]$ , whereas that corresponding to snow images is  $[0, 0, 1, 0, 0, 0, 0, 0]$ . Next, we elaborate on the usage of the predefined one-hot noise indicators.

Taking a RGB image  $I_{in}$  as input, ResNet-50 maps it into high-dimensional feature representation:

$$\{\hat{F}_1, \hat{F}_2, \hat{F}_3, \hat{F}_4, \hat{F}_5\} = \mathcal{T}_{resnet}(I_{in}) \quad (1)$$

where  $\mathcal{T}_{resnet}(\cdot)$  denotes the feature extraction operation, and  $\hat{F}_i$  denotes the semantic feature of the  $i$ -th stage ( $S_i$ ) extracted by the pure ResNet-50.

To integrate this noise indicator into the backbone network, we design a dedicated module termed the noise indicator fusion module (NIFM). As illustrated in Fig. 2, NIFMs are inserted between every two adjacent stages of the backbone network. Taking the first NIFM (positioned after the backbone's first stage,  $S_1$ ) as an example, the inputs consist of two components: the semantic feature  $F_1$  extracted from the input image  $I_{in}$  after  $S_1$  of the backbone network, and the pre-constructed noise indicator  $T$ . The semantic feature  $F_1$  is compressed into a one-dimensional vector via a global average pooling layer (GAP), which is then concatenated with the noise indicator to form a combined feature representation:

$$F_1^T = \text{Concat}(\text{GAP}(\hat{F}_1), T) \quad (2)$$

where  $\text{Concat}(\cdot, \cdot)$  denotes the channel-wise concatenation operation. Next, the concatenated feature  $F_1^T$  is fed into two fully connected layers ( $fc$ ) to learn a noise indicator weight  $W_1$ . This weight vector encodes the degree to which the backbone's features should be adjusted to counteract the specific noise type indicated by  $T$ . The weight calculation is formulated as:

$$W_1 = \sigma(fc_2(\text{relu}(fc_1(F_1^T)))) \quad (3)$$

where  $\sigma(\cdot)$  denotes the sigmoid operation. Finally, the learned weight  $W_1$  is applied to modulate the backbone network, thereby incorporating noise-aware conditioning and producing the enhanced output feature  $F_1$  of the first stage:

$$F_1 = W_1 \otimes \hat{F}_1 \quad (4)$$

where  $\otimes$  denotes the channel-wise multiplication. It can be seen that  $W_1$  implements the switching of noise types for the features  $\hat{F}_1$ . The same operational logic extends to all

subsequent NIFMs. For the  $n$ -th NIFM (where  $n = 2, 3, 4$ ), the inputs are the semantic feature  $\hat{F}_n$  (extracted from the backbone's  $n$ -th stage,  $S_n$ ) and the noise indicator  $T$ . In this manner, both the noise-specific features and their associated indicator weights are progressively derived for the remaining stages. From Eq. (1), we can formulate the multi-scale semantic feature extraction of the NIFM-integrated backbone network as:

$$\{F_1, F_2, F_3, F_4, F_5\} = \mathcal{T}_{resnet}^{NIFM}(I_{in}) \quad (5)$$

where  $\mathcal{T}_{resnet}^{NIFM}(\cdot)$  denotes the NIFM-augmented ResNet-50, *i.e.*, the specific encoder.

### C. Decoders

Mainstream backbone-based SOD methods can generally be decomposed into two core components: an encoder and a decoder. The encoder is engineered to extract multi-scale semantic features, while decoders, distinguished by diverse architectural designs (*e.g.*, pyramid feature fusion, cross-scale attention, or residual refinement modules), are tasked with progressively mapping these hierarchical semantic features into dense, pixel-wise saliency maps. To validate the effectiveness and generalization of the proposed specific encoder, we conduct experiments by pairing this encoder with decoders from seven representative SOD models that cover different architectural paradigms. These models include F3Net [74], R-Net [75], MINET [37], AESINet [76], BAFSNet [77], DC-Net [78] and EDN [79]. To ensure a fair comparison, all models adopt the same loss function and retain original multi-scale supervision mechanisms. Taking the single-scale supervision as an example, the loss function can be formulated as follows:

$$\mathcal{L}_{total} = \mathcal{L}_{bce} + \mathcal{L}_{ssim} + \mathcal{L}_{iou} \quad (6)$$

where  $\mathcal{L}_{bce}$ ,  $\mathcal{L}_{ssim}$  and  $\mathcal{L}_{iou}$  denote BCE loss [84], SSIM loss [85] and IoU loss [86], respectively. The calculation process of each loss function is as follows:

$$\begin{cases} \mathcal{L}_{bce} = -I_{gt} \cdot \log(I_{out}) + (I_{gt} - 1) \cdot \log(1 - I_{out}) \\ \mathcal{L}_{ssim} = 1 - \frac{(2\mu_{I_{gt}}\mu_{I_{out}} + C_1)(2\sigma_{I_{gt}I_{out}} + C_2)}{(\mu_{I_{gt}}^2 + \mu_{I_{out}}^2 + C_1)(\sigma_{I_{gt}}^2 + \sigma_{I_{out}}^2 + C_2)} \\ \mathcal{L}_{iou} = 1 - \frac{I_{gt} \cdot I_{out}}{I_{gt} + I_{out} - I_{gt} \cdot I_{out}} \end{cases} \quad (7)$$

where  $I_{out}$  and  $I_{gt}$  denote the predicted saliency map and ground-truth.  $\mu_{I_{out}}$ ,  $\mu_{I_{gt}}$  and  $\sigma_{I_{out}}$ ,  $\sigma_{I_{gt}}$  are the mean and standard deviations of  $I_{out}$  and  $I_{gt}$  respectively,  $\sigma_{I_{gt}I_{out}}$  is their covariance,  $C_1 = 0.012$  and  $C_2 = 0.032$  are used to avoid dividing by 0.

### D. Discussion

With the rapid advancement of computer vision, researchers have devoted growing attention to the algorithmic application for low-quality scenarios. These efforts have motivated us to develop a frameworks for achieving robust SOD under diverse weather conditions. In parallel, recent progress in the SOD field has explored the settings of various modal inputs to improve the generalization capability of models. To realize this, existing methods incorporate modality indicators

TABLE I  
STATISTICS OF THE WXSOD DATASET.

WXSOD												
100% Training set									50% Training set	30% Training set	Synthesized test set	Real test set
Clean	Rain	Snow	Fog	Light	Dark	Rain&Snow	Rain&Fog	Snow&Fog				
631	1524	1547	1534	1531	1535	1494	1562	1533	6445	3867	1500	554

TABLE II  
MODEL PERFORMANCE COMPARISONS USING 100% TRAINING SET. THE UPPER SECTION PRESENTS RESULTS ON THE SYNTHESIZED TEST SET, WHILE THE LOWER SECTION REPORTS RESULTS ON THE REAL TEST SET. FOUR MODELS (A3Net [87], HDNet [88], ICONet [89], TCGNet [90]) WITH PURPLE BACKGROUND COLOR ADOPT DEFAULT STRUCTURE.

Test set	Methods	NIFM	$MAE \downarrow$		$S \uparrow$		$F_{\beta}^{adv} \uparrow$		$F_{\beta}^{mean} \uparrow$		$F_{\beta}^{max} \uparrow$		$E_{\xi}^{adv} \uparrow$		$E_{\xi}^{mean} \uparrow$		$E_{\xi}^{max} \uparrow$		MACs(G)	Params(M)	FPS
			val	$\Delta$	val	$\Delta$	val	$\Delta$	val	$\Delta$	val	$\Delta$	val	$\Delta$	val	$\Delta$	val	$\Delta$			
Sys	A3Net	-	0.0327	-	0.8784	-	0.8158	-	0.8286	-	0.8472	-	0.9176	-	0.9131	-	0.9253	-	22.70	27.94	228.08
	HDNet	-	0.0397	-	0.8537	-	0.7875	-	0.7964	-	0.8162	-	0.8990	-	0.8901	-	0.9053	-	24.67	26.19	196.14
	ICONet	-	0.0433	-	0.8411	-	0.7496	-	0.7704	-	0.7957	-	0.8924	-	0.8908	-	0.9078	-	33.03	24.95	270.19
	TCGNet	-	0.0317	-	0.8832	-	0.8278	-	0.8388	-	0.8576	-	0.9228	-	0.9180	-	0.9288	-	70.26	60.14	52.84
	F3Net	✓	0.0353	-	0.8735	-	0.8111	-	0.8228	-	0.8434	-	0.9134	-	0.9092	-	0.9212	-	19.63	25.54	158.00
	✓	0.0307	13.03%	0.8822	0.99%	0.8346	2.90%	0.8422	2.36%	0.8583	1.77%	0.9272	1.51%	0.9210	1.29%	0.9309	1.06%	19.64	26.93	155.37	
	MINET	✓	0.0349	-	0.8721	-	0.8169	-	0.8219	-	0.8417	-	0.9165	-	0.9110	-	0.9206	-	125.43	162.38	47.20
	✓	0.0324	7.16%	0.8772	0.58%	0.8197	0.34%	0.8273	0.65%	0.8461	0.52%	0.9212	0.52%	0.9140	0.33%	0.9233	0.28%	125.44	163.77	45.43	
	EDN	✓	0.0335	-	0.8779	-	0.8114	-	0.8280	-	0.8497	-	0.9138	-	0.9084	-	0.9227	-	20.41	42.85	93.96
	✓	0.0317	5.37%	0.8827	0.54%	0.8154	0.49%	0.8337	0.70%	0.8539	0.49%	0.9185	0.51%	0.9145	0.67%	0.9279	0.57%	20.42	44.23	93.67	
	AESINet	✓	0.0328	-	0.8691	-	0.8254	-	0.8292	-	0.8366	-	0.9197	-	0.9140	-	0.9190	-	45.54	51.57	50.95
	✓	0.0314	4.27%	0.8714	0.26%	0.8276	0.26%	0.8306	0.17%	0.8380	0.17%	0.9219	0.25%	0.9160	0.22%	0.9213	0.25%	45.55	52.96	50.73	
	BAFSNet	✓	0.0315	-	0.8825	-	0.8347	-	0.8404	-	0.8561	-	0.9280	-	0.9199	-	0.9300	-	34.44	31.44	74.29
	✓	0.0298	5.40%	0.8857	0.36%	0.8338	-0.10%	0.8422	0.22%	0.8607	0.54%	0.9323	0.46%	0.9273	0.80%	0.9380	0.86%	34.45	32.82	72.63	
	DC-Net	✓	0.0321	-	0.8827	-	0.8341	-	0.8399	-	0.8558	-	0.9277	-	0.9207	-	0.9321	-	120.21	88.94	39.67
	✓	0.0315	1.87%	0.8817	-0.11%	0.8323	-0.22%	0.8382	-0.20%	0.8527	-0.37%	0.9245	-0.35%	0.9153	-0.59%	0.9267	-0.59%	120.22	89.29	37.42	
	R-Net	✓	0.0372	-	0.8668	-	0.8152	-	0.8221	-	0.8379	-	0.9124	-	0.9068	-	0.9163	-	48.72	98.00	59.22
	✓	0.0329	11.56%	0.8762	1.08%	0.8215	0.78%	0.8313	1.11%	0.8481	1.22%	0.9177	0.59%	0.9144	0.83%	0.9222	0.65%	48.73	99.39	58.57	
	Average	✓	0.0339	-	0.8749	-	0.8212	-	0.8292	-	0.8459	-	0.9188	-	0.9129	-	0.9231	-	-	-	-
	✓	0.0315	7.12%	0.8796	0.53%	0.8264	0.63%	0.8351	0.71%	0.8511	0.62%	0.9233	0.50%	0.9175	0.51%	0.9272	0.44%	-	-	-	
Real	A3Net	-	0.0263	-	0.8909	-	0.8172	-	0.8350	-	0.8586	-	0.9207	-	0.9199	-	0.9329	-	22.70	27.94	228.08
	HDNet	-	0.0266	-	0.8938	-	0.8179	-	0.8447	-	0.8734	-	0.9219	-	0.9219	-	0.9361	-	24.67	26.19	196.14
	ICONet	-	0.0327	-	0.8619	-	0.7595	-	0.7885	-	0.8209	-	0.9007	-	0.9117	-	0.9276	-	33.03	24.95	270.19
	TCGNet	-	0.0185	-	0.9185	-	0.8529	-	0.8739	-	0.8992	-	0.9429	-	0.9476	-	0.9594	-	70.26	60.14	52.84
	F3Net	✓	0.0248	-	0.8982	-	0.8141	-	0.8375	-	0.8633	-	0.9147	-	0.9198	-	0.9344	-	19.63	25.54	158.00
	✓	0.0196	20.97%	0.9133	1.68%	0.8378	2.91%	0.8611	2.82%	0.8951	3.68%	0.9315	1.85%	0.9383	2.01%	0.9531	2.00%	19.64	26.93	155.37	
	MINET	✓	0.0232	-	0.9007	-	0.8269	-	0.8470	-	0.8841	-	0.9233	-	0.9282	-	0.9471	-	125.43	162.38	47.20
	✓	0.0241	-3.88%	0.9038	0.35%	0.8240	-0.36%	0.8445	-0.30%	0.8816	-0.28%	0.9207	-0.28%	0.9250	-0.35%	0.9395	-0.80%	125.44	163.77	45.43	
	EDN	✓	0.0223	-	0.9097	-	0.8140	-	0.8520	-	0.8848	-	0.9158	-	0.9272	-	0.9430	-	20.41	42.85	93.96
	✓	0.0183	17.94%	0.9173	0.85%	0.8204	0.78%	0.8634	1.34%	0.8945	1.09%	0.9221	0.68%	0.9395	1.33%	0.9554	1.32%	20.42	44.23	93.67	
	AESINet	✓	0.0253	-	0.8916	-	0.8283	-	0.8441	-	0.8657	-	0.9266	-	0.9297	-	0.9370	-	45.54	51.57	50.95
	✓	0.0179	29.25%	0.9097	2.03%	0.8569	3.45%	0.8694	2.99%	0.8834	2.04%	0.9418	1.64%	0.9441	1.55%	0.9501	1.40%	45.55	52.96	50.73	
	BAFSNet	✓	0.0198	-	0.9088	-	0.8427	-	0.8565	-	0.8768	-	0.9311	-	0.9307	-	0.9405	-	34.44	31.44	74.29
	✓	0.0197	0.51%	0.9132	0.48%	0.8395	-0.37%	0.8620	0.64%	0.8913	1.65%	0.9350	0.42%	0.9395	0.95%	0.9534	1.37%	34.45	32.82	72.63	
	DC-Net	✓	0.0261	-	0.8960	-	0.8232	-	0.8444	-	0.8767	-	0.9224	-	0.9249	-	0.9399	-	120.21	88.94	39.67
	✓	0.0194	25.67%	0.9079	1.32%	0.8446	2.60%	0.8611	1.97%	0.8842	0.86%	0.9332	1.16%	0.9356	1.15%	0.9481	0.87%	120.22	89.29	37.42	
	R-Net	✓	0.0260	-	0.8938	-	0.8223	-	0.8383	-	0.8655	-	0.9209	-	0.9220	-	0.9336	-	48.72	98.00	59.22
	✓	0.0189	27.31%	0.9150	2.37%	0.8483	3.16%	0.8663	3.35%	0.8969	3.62%	0.9408	2.15%	0.9434	2.32%	0.9566	2.47%	48.73	99.39	58.57	
	Average	✓	0.0239	-	0.8998	-	0.8245	-	0.8457	-	0.8739	-	0.9221	-	0.9261	-	0.9394	-	-	-	-
	✓	0.0197	17.67%	0.9114	1.29%	0.8388	1.73%	0.8611	1.82%	0.8896	1.80%	0.9321	1.09%	0.9379	1.28%	0.9509	1.23%	-	-	-	

or learnable prompts to guide a single backbone network in adapting to input images of multiple modalities, thereby eliminating the need for separate network architectures for different modalities. Such technical designs provide valuable insights for our research. However, a fundamental distinction must be clarified: images captured under complex weather conditions (e.g., rain, fog or snow) inherently belong to the same visual modality. This implies that the conventional SOD model can technically process weather-corrupted images without additional modifications, albeit with suboptimal performance. Therefore, the focus of our work is the design of an encoder. Concretely, we employ a simple yet effective NIFM to enhance the backbone network’s capability of extracting features from images corrupted by different types of weather-induced noise, while ensuring compatibility with existing decoders. The experimental section will verify that introducing noise indicators can optimize the spatial distribution of images with different types of noise, promoting the mutual proximity of image features with the same noise category.

## IV. EXPERIMENT

### A. Datasets and Evaluation Metrics

1) *Datasets*: Experiments are conducted on the WXSOD dataset [47], a dedicated SOD benchmark for adverse weather conditions. As detailed in Table I, the original WXSOD comprises 12,891 images for training, 1,500 synthesized and 554 real images for testing. Notably, the 12,891 training samples can be further categorized into 9 subsets based on weather conditions, including Clean (631 images), Rain (1524 images), Snow (1547 images), Fog (1534 images), Light (1531 images), Dark (1535 images), Rain&Snow (1494 images), Rain&Fog (1562 images), and Snow&Fog (1533 images). It is emphasized that the scenes within each subset are unique. By using subsets for training, we can evaluate the model detection performance under specific weather noise. To further verify the effectiveness of our framework across datasets of varying scales, we generate two additional training subsets by randomly filtering the original training set at two different ratios: 50% and 30%. These filtered subsets are denoted as the “50% Training set” (containing 6,445 images) and the “30% Training set” (containing 3,867 images), respectively. This experimental setup allows us to analyze how the performance

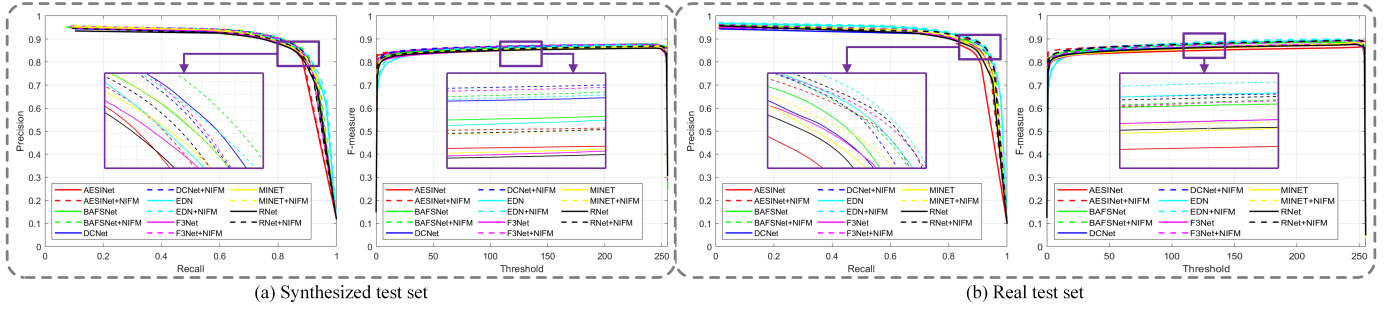


Fig. 3. Quantitative evaluation of different saliency models: (a) presents PR curves and F-measure curves on the synthesized test set, while (b) presents PR curves and F-measure curves on the real test set.

of the framework changes as the amount of training data decreases, thereby evaluating the effectiveness of the framework.

2) *Evaluation Metrics*: Adhering to WFANet [47], we employ ten commonly used evaluation metrics, which are listed as follows: mean absolute error ( $MAE$ ) [91], S-measure ( $S$ ) [92], F-measure ( $F_{\beta}^{adv}$ ,  $F_{\beta}^{mean}$ ,  $F_{\beta}^{max}$ ) [93], E-measure ( $E_{\xi}^{adv}$ ,  $E_{\xi}^{mean}$ ,  $E_{\xi}^{max}$ ) [94], F-measure curve and Precision-Recall (PRcurve) [93]. These metrics evaluate the model's performance from multiple aspects, such as pixel-level error, structural consistency, and overall perceptual quality, thereby ensuring the comprehensiveness and reliability of the evaluation results.

To quantify additional computational costs incurred by the combinations of various decoders and the basic network, we report the number of learnable parameters (Params), multiply-accumulate operations (MACs) and frames per second (FPS). Note that the MACs and FPS are measured on a  $384 \times 384$  image, using an NVIDIA P100 GPU.

### B. Implementation Details

The basic framework employs a ResNet-50 as the encoder, with the NIFM embedded into adjacent stages of the encoder. In contrast, the decoder leverages existing network architectures. During the training phase, the Adam optimizer ( $\beta_1 = 0.9$  and  $\beta_2 = 0.999$ ) is utilized to update network parameters with an initial learning rate of 0.001. To ensure stable convergence, the StepLR learning rate scheduling strategy is employed, where the learning rate is decayed by a factor of  $\gamma = 0.2$  every 40 epochs. All input images are uniformly resized to  $384 \times 384$  resolution and processed in mini-batches of 4 over 52 epochs. The framework adopts a unified loss function when applying different decoders, but retains multi-scale loss supervision that reported in the corresponding original literature.

### C. Comparison with SOTA Models

1) *Quantitative Comparison*: To comprehensively validate the effectiveness of the proposed framework, particularly the specific encoder integrated with the NIFM, quantitative experiments are conducted from two perspectives: 1) the effectiveness of the proposed framework when paired with different decoder configurations; 2) the effectiveness of the proposed framework under varying dataset scales.

As presented in Table II, we report the results of models integrated with seven decoders (*i.e.*, F3Net [74], R-Net [75], MINET [37], AESINet [76], BAFSNet [77], DC-Net [78] and EDN [79]) on both synthesized and real test set of WXSOD. Herein, "NIFM-✗" denotes models adopting the conventional ResNet-50 encoder, while "NIFM-✓" indicates models equipped with the specific encoder (integrated with the noise indicator fusion module, NIFM). Quantitative analysis reveals that after replacing the conventional encoder with our specific encoder, the average MAE across all seven models is reduced by 7.12% on the synthesized test set and by 17.67% on the real test set, respectively. Beyond MAE, consistent performance enhancements are also observed across other evaluation metrics, with greater improvement on the real test set compared to the synthesized one. This discrepancy highlights the specific encoder's stronger ability to mitigate real weather noise, which exhibits more complex and unstructured characteristics than synthetic noise. Furthermore, Table II also summarizes the variations in the computational cost (MACs, Params and FPS) for models before and after embedding the NIFM. It is evident that NIFM is a lightweight module, increasing parameters by less than 2M and adding only 0.01G MACs. Collectively, these results confirm that the proposed NIFM-enhanced specific encoder effectively boosts model performance with negligible computational cost, which is a core advantage for algorithm deployment.

We have provided additional experimental results for four models in Table II. Taking F3Net as an example, after injecting NIFM, the model performance using F3Net encoder surpasses TCGNet and A3Net, which also proves the effectiveness of our framework.

For comprehensive quantitative evaluation, Fig. 3 presents Precision-Recall (PR) and F-measure curves, which compare the performance of models formed by pairing two types of encoders (the conventional encoder and our NIFM-enhanced encoder) with seven distinct decoders. A consistent trend can be observed across all decoder configurations: under the same decoder setup, the PR curve of the model equipped with the NIFM-enhanced encoder lies closer to the top-right corner, and the area below the F-measure curve is also larger than that of the model with the conventional encoder. These experiments results prove the effectiveness and superiority of our proposed NIFM-enhanced encoder.

To further evaluate the stability of the proposed framework

TABLE III

MODEL PERFORMANCE COMPARISONS USING 50% AND 30% TRAINING SET, RESPECTIVELY. THE UPPER SECTION PRESENTS RESULTS ON THE 50% TEST SET, WHILE THE LOWER SECTION REPORTS RESULTS ON THE 30% TEST SET.

Ratio	Test set	Decoders	NIFM	$MAE \downarrow$		$S \uparrow$		$F_{\beta}^{adv} \uparrow$		$F_{mean}^{adv} \uparrow$		$F_{\beta}^{max} \uparrow$		$E_{\xi}^{adv} \uparrow$		$E_{mean}^{adv} \uparrow$		$E_{\xi}^{max} \uparrow$		
				val	$\Delta$	val	$\Delta$	val	$\Delta$	val	$\Delta$	val	$\Delta$	val	$\Delta$	val	$\Delta$	val	$\Delta$	
50%	Sys	F3Net	✗	0.0391	—	0.8640	—	0.7946	—	0.8060	—	0.8240	—	0.9033	—	0.8991	—	0.9102	—	
		✓	0.0343	12.28%	0.8737	1.13%	0.8133	2.35%	0.8219	1.97%	0.8399	1.93%	0.9150	1.30%	0.9098	1.19%	0.9211	1.19%		
		MINET	✗	0.0372	—	0.8681	—	0.7916	—	0.8123	—	0.8342	—	0.9014	—	0.9061	—	0.9173	—	
		✓	0.0366	1.61%	0.8670	-0.14%	0.8067	1.91%	0.8142	0.24%	0.8339	-0.04%	0.9131	1.29%	0.9074	0.14%	0.9159	-0.15%		
		EDN	✗	0.0363	—	0.8733	—	0.8002	—	0.8201	—	0.8405	—	0.9058	—	0.9015	—	0.9197	—	
		✓	0.0352	3.03%	0.8726	-0.09%	0.8038	0.45%	0.8199	-0.02%	0.8394	-0.13%	0.9079	0.23%	0.9050	0.38%	0.9198	0.01%		
		AESINet	✗	0.0398	—	0.8480	—	0.7878	—	0.7896	—	0.7895	—	0.8970	—	0.8919	—	0.8971	—	
		✓	0.0381	4.27%	0.8534	0.64%	0.8054	2.23%	0.8079	2.33%	0.8159	2.18%	0.9051	0.91%	0.8990	0.79%	0.9045	0.83%		
		BAFSNet	✗	0.0336	—	0.8741	—	0.8144	—	0.8282	—	0.8487	—	0.9149	—	0.9125	—	0.9226	—	
		✓	0.0323	3.87%	0.8759	0.20%	0.8173	0.35%	0.8291	0.11%	0.8490	0.03%	0.9202	0.58%	0.9194	0.76%	0.9289	0.69%		
		DC-Net	✗	0.0351	—	0.8751	—	0.8189	—	0.8262	—	0.8427	—	0.9164	—	0.9085	—	0.9197	—	
		✓	0.0323	7.98%	0.8826	0.86%	0.8330	1.73%	0.8411	1.81%	0.8597	2.02%	0.9242	0.86%	0.9200	1.26%	0.9303	1.16%		
	R-Net	✗	0.0354	—	0.8724	—	0.8143	—	0.8233	—	0.8428	—	0.9168	—	0.9110	—	0.9220	—		
	✓	0.0373	-5.37%	0.8692	-0.37%	0.8003	-1.72%	0.8106	-1.54%	0.8302	-1.50%	0.9048	-1.31%	0.9035	-0.83%	0.9118	-1.11%			
	Average	✗	0.0366	—	0.8679	—	0.8031	—	0.8151	—	0.8331	—	0.9080	—	0.9044	—	0.9155	—		
	✓	0.0352	4.05%	0.8706	0.32%	0.8114	1.03%	0.8207	0.69%	0.8383	0.63%	0.9129	0.55%	0.9092	0.53%	0.9189	0.37%			
	Real	F3Net	✗	0.0312	—	0.8870	—	0.7973	—	0.8237	—	0.8515	—	0.9055	—	0.9097	—	0.9250	—	
		✓	0.0209	33.01%	0.9102	2.61%	0.8379	5.10%	0.8574	4.08%	0.8860	4.05%	0.9337	3.12%	0.9354	2.82%	0.9467	2.34%		
		MINET	✗	0.0341	—	0.8769	—	0.7829	—	0.8058	—	0.8478	—	0.8968	—	0.9032	—	0.9219	—	
		✓	0.0260	23.75%	0.8986	2.47%	0.8244	5.30%	0.8421	4.50%	0.8726	2.93%	0.9177	2.33%	0.9208	1.94%	0.9346	1.38%		
		EDN	✗	0.0266	—	0.9022	—	0.7867	—	0.8407	—	0.8755	—	0.8953	—	0.9199	—	0.9387	—	
		✓	0.0222	16.54%	0.9072	0.55%	0.8109	3.08%	0.8472	0.77%	0.8825	0.80%	0.9143	2.12%	0.9286	0.94%	0.9457	0.75%		
		AESINet	✗	0.0263	—	0.8859	—	0.8158	—	0.8289	—	0.8482	—	0.9209	—	0.9237	—	0.9324	—	
		✓	0.0209	20.53%	0.9020	1.81%	0.8438	3.43%	0.8583	3.56%	0.8752	3.18%	0.9346	1.49%	0.9384	1.59%	0.9441	1.26%		
		BAFSNet	✗	0.0232	—	0.8990	—	0.8176	—	0.8406	—	0.8728	—	0.9214	—	0.9272	—	0.9423	—	
		✓	0.0199	14.22%	0.9074	0.93%	0.8299	1.51%	0.8521	1.38%	0.8883	1.78%	0.9282	0.75%	0.9343	0.77%	0.9517	1.00%		
		DC-Net	✗	0.0338	—	0.8880	—	0.8029	—	0.8335	—	0.8602	—	0.9026	—	0.9115	—	0.9233	—	
		✓	0.0261	22.78%	0.9006	1.41%	0.8341	3.89%	0.8531	2.35%	0.8849	2.87%	0.9257	2.56%	0.9282	1.84%	0.9451	2.36%		
		R-Net	✗	0.0281	—	0.8955	—	0.8236	—	0.8422	—	0.8636	—	0.9172	—	0.9184	—	0.9287	—	
		✓	0.0238	15.30%	0.9032	0.86%	0.8274	0.46%	0.8442	0.23%	0.8729	1.07%	0.9285	1.23%	0.9288	1.14%	0.9406	1.27%		
		Average	✗	0.0290	—	0.8907	—	0.8038	—	0.8308	—	0.8599	—	0.9085	—	0.9162	—	0.9303	—	
		✓	0.0228	21.40%	0.9042	1.51%	0.8298	3.23%	0.8506	2.39%	0.8803	2.37%	0.9261	1.94%	0.9306	1.57%	0.9441	1.48%		
30%		Sys	F3Net	✗	0.0384	—	0.8588	—	0.7942	—	0.7991	—	0.8177	—	0.9056	—	0.8926	—	0.9083	—
			✓	0.0380	1.04%	0.8687	1.15%	0.8100	1.99%	0.8173	2.28%	0.8348	2.09%	0.9123	0.75%	0.9050	1.38%	0.9180	1.06%	
			MINET	✗	0.0432	—	0.8553	—	0.7955	—	0.8051	—	0.8264	—	0.9007	—	0.8969	—	0.9103	—
			✓	0.0384	11.11%	0.8601	0.57%	0.8047	1.15%	0.8100	0.61%	0.8270	0.07%	0.9102	1.05%	0.9016	0.52%	0.9141	0.41%	
	EDN		✗	0.0370	—	0.8668	—	0.7939	—	0.8117	—	0.8337	—	0.9036	—	0.8951	—	0.9177	—	
	✓		0.0371	-0.27%	0.8693	0.29%	0.7897	-0.53%	0.8109	-0.10%	0.8323	-0.17%	0.9021	-0.17%	0.9023	0.80%	0.9167	-0.11%		
	AESINet		✗	0.0421	—	0.8410	—	0.7780	—	0.7817	—	0.7921	—	0.8903	—	0.8885	—	0.8935	—	
	✓		0.0362	14.01%	0.8551	1.68%	0.8011	2.97%	0.8039	2.84%	0.8119	2.50%	0.9083	2.02%	0.9004	1.35%	0.9053	1.32%		
	BAFSNet		✗	0.0357	—	0.8680	—	0.8062	—	0.8185	—	0.8381	—	0.9149	—	0.9116	—	0.9211	—	
	✓		0.0348	2.52%	0.8713	0.38%	0.8144	1.03%	0.8236	0.63%	0.8415	0.41%	0.9150	0.01%	0.9104	-0.14%	0.9199	-0.13%		
	DC-Net		✗	0.0375	—	0.8637	—	0.8040	—	0.8118	—	0.8274	—	0.9101	—	0.9007	—	0.9136	—	
	✓		0.0348	7.20%	0.8707	0.81%	0.8128	1.10%	0.8223	1.30%	0.8400	1.52%	0.9158	0.63%	0.9096	1.00%	0.9206	0.76%		
	R-Net	✗	0.0416	—	0.8484	—	0.7877	—	0.7925	—	0.8100	—	0.9000	—	0.8868	—	0.8988	—		
	✓	0.0395	5.05%	0.8620	1.60%	0.7978	1.29%	0.8066	1.78%	0.8254	1.90%	0.9057	0.63%	0.8987	1.35%	0.9108	1.34%			
	Average	✗	0.0394	—	0.8574	—	0.7942	—	0.8029	—	0.8208	—	0.9036	—	0.8960	—	0.9090	—		
	✓	0.0370	6.06%	0.8653	0.92%	0.8044	1.28%	0.8135	1.32%	0.8304	1.17%	0.9099	0.70%	0.9040	0.89%	0.9150	0.66%			
	Real	F3Net	✗	0.0324	—	0.8836	—	0.7998	—	0.8115	—	0.8428	—	0.9006	—	0.9030	—	0.9210	—	
		✓	0.0273	15.74%	0.8994	1.79%	0.8187	3.66%	0.8399	3.51%	0.8731	3.59%	0.9197	2.12%	0.9233	2.25%	0.9381	1.86%		
		MINET	✗	0.0339	—	0.8707	—	0.7876	—	0.8057	—	0.8377	—	0.9060	—	0.9057	—	0.9197	—	
		✓	0.0282	16.81%	0.8892	2.12%	0.8121	3.11%	0.8282	2.79%	0.8640	3.15%	0.9114	0.59%	0.9129	0.80%	0.9286	0.97%		
		EDN	✗	0.0248	—	0.9036	—	0.7841	—	0.8392	—	0.8712	—	0.8970	—	0.9210	—	0.9427	—	
		✓	0.0263	-6.05%	0.8978	-0.63%	0.7945	1.32%	0.8299	-1.12%	0.8644	-0.78%	0.9046	0.85%	0.9207	-0.03%	0.9412	-0.16%		
		AESINet	✗	0.0287	—	0.8830	—	0.8087	—	0.8216	—	0.8496	—	0.9116	—	0.9148	—	0.9286	—	
		✓	0.0241	16.03%	0.8884	0.61%	0.8193	1.31%	0.8323	1.31%	0.8545	0.57%	0.9214	1.08%	0.9203	0.60%	0.9294	0.10%		
		BAFSNet	✗	0.0242	—	0.8975	—	0.8165	—	0.8374	—	0.8671	—	0.9202	—	0.9263	—	0.9388	—	
		✓	0.0218	9.92%	0.9075	1.12%	0.8337	2.11%	0.8530	1.86%	0.8822	1.74%	0.9315	1.23%	0.9355	1.00%	0.9480	0.98%		
		DC-Net	✗	0.0278	—	0.8931	—	0.8200	—	0.8362	—	0.8579	—	0.9186	—	0.9161	—	0.9301	—	
		✓	0.0262	5.76%	0.9017	0.96%	0.8278	0.96%	0.8467	1.26%	0.8734	1.81%	0.9248	0.67%	0.9241	0.87%	0.9355	0.58%		
		R-Net	✗	0.0305	—	0.8905	—	0.8053	—	0.8272	—	0.8589	—	0.9142	—	0.9150	—	0.9292	—	
		✓	0.0272	10.82%	0.8991	0.96%	0.8047	-0.07%	0.8315	0.51%	0.8650	0.70%	0.9107	-0.38%	0.9187	0.41%	0.9358	0.72%		
		Average	✗	0.0289	—	0.8889	—	0.8017	—	0.8255	—	0.8550	—	0.9098	—	0.9146	—	0.9300	—	
		✓	0.0259	10.48%	0.8976	0.98%	0.8158	1.76%												

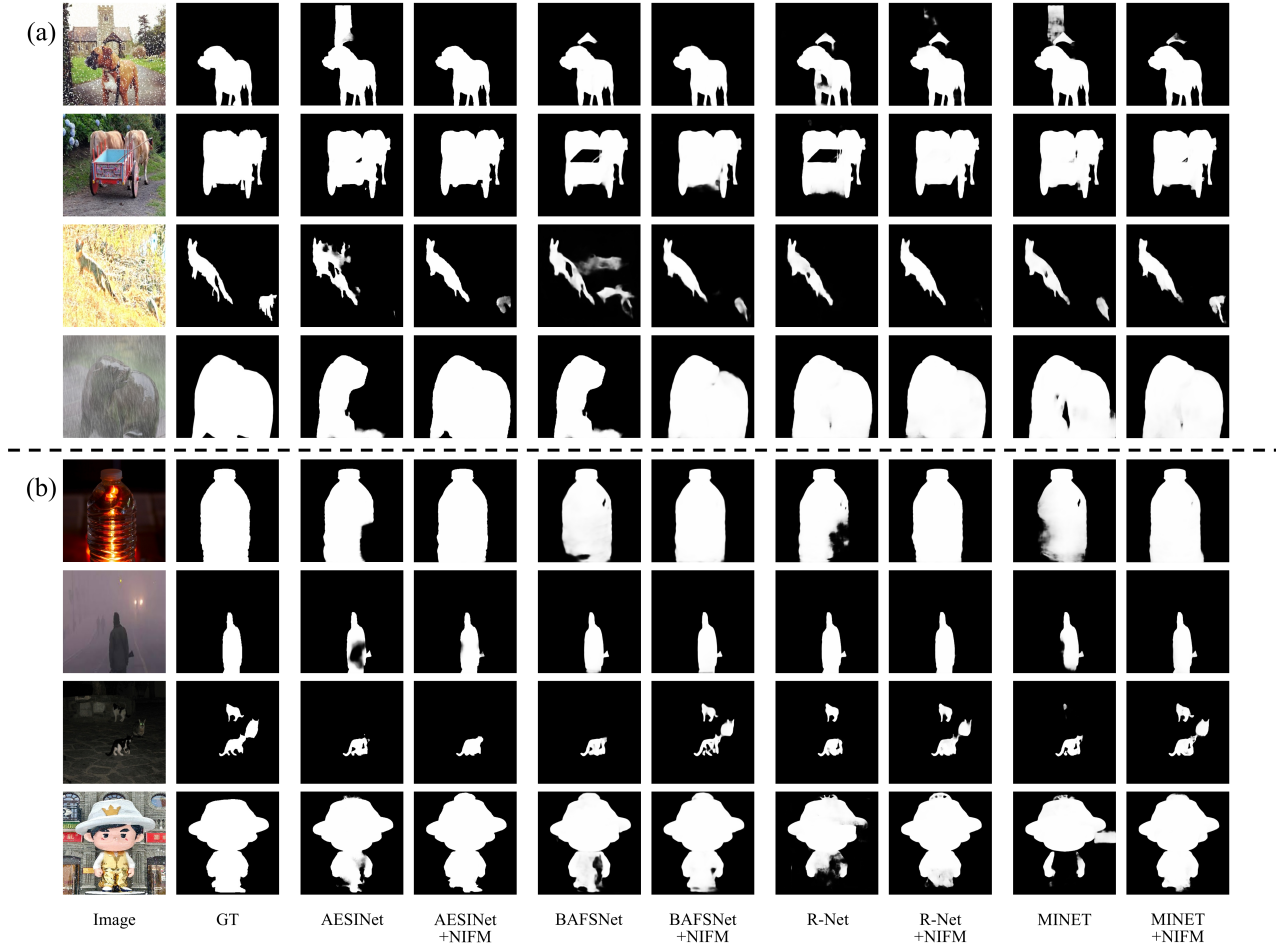


Fig. 4. Visual comparison under different decoder settings. (a) Visualization results on the synthesized test set. (b) Visualization results on the real test set.

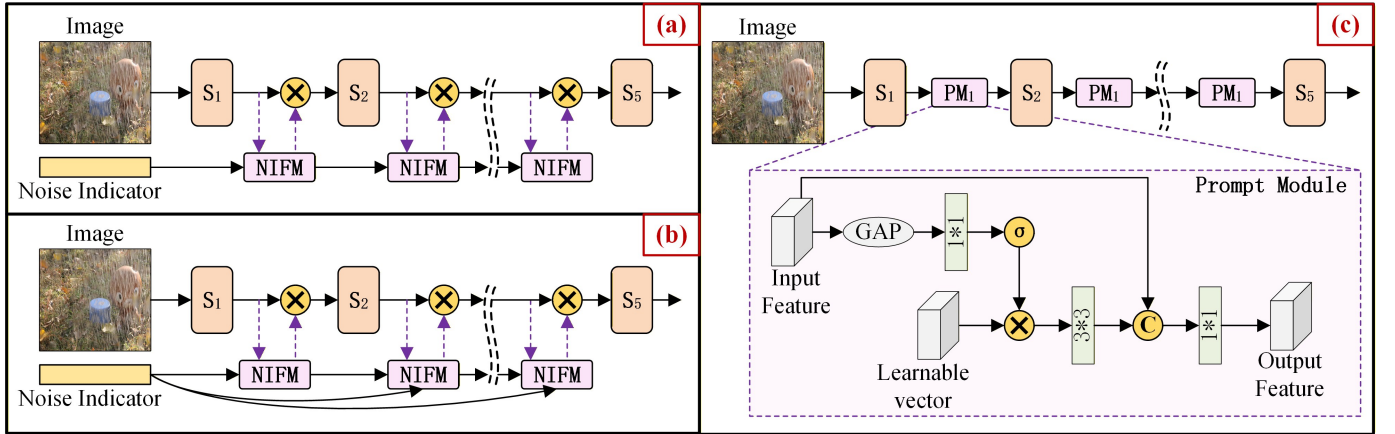


Fig. 5. Two schemes for integrating the SOD framework with NIFM.

the saliency prediction results of models configured with either the conventional encoder (baseline) or the specific encoder (denoted as “+NIFM”), paired with four decoders (AESINet, BAFSNet, Rnet, and F3Net). It can be observed that the integration of NIFM yields more complete prediction results, demonstrating inherent robustness against weather-induced noise. For example, in the first row of Fig. 4(b), the contour of

the bottle is blurred by low light. As a result, the model with the conventional encoder can only detect partial regions of the bottle with relatively high contrast. In contrast, the model integrated with NIFM produces a more complete detection.

To verify the regulatory effect of NIFM on feature distributions, we visualized the feature distributions of various models using the t-SNE algorithm as shown in Fig. 6. Exper-

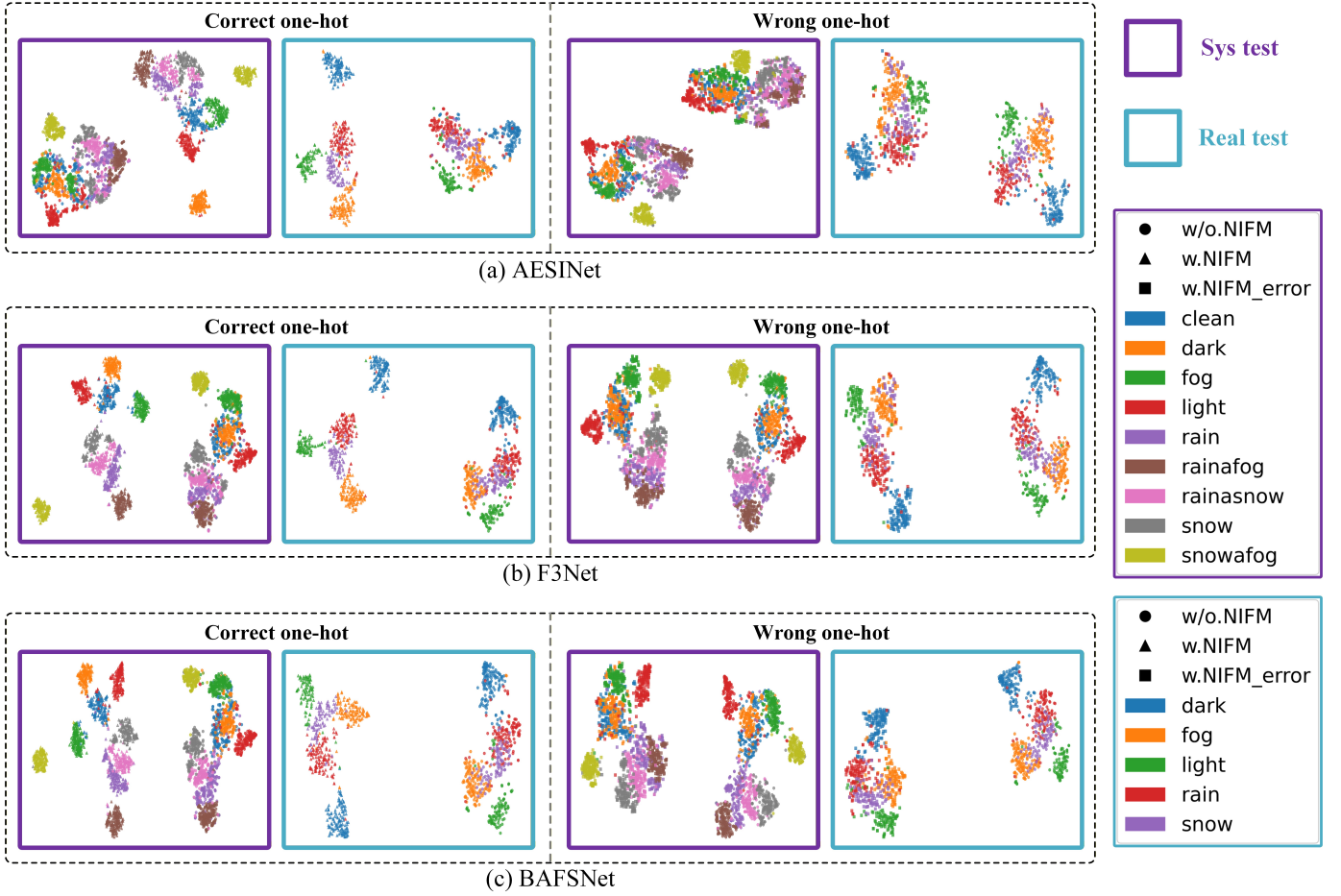


Fig. 6. Visualization of output features from different models via t-SNE. Purple boxes denote results from the synthetic test set while blue boxes denote those from the real test set. Circular features are derived from models without NIFM, square features from models with incorrectly configured one-hot encoding, and triangular features represent complete models with correctly configured one-hot encoding.

iments under three decoder settings demonstrate that models incorporating NIFM with correct one-hot vectors achieve more distinct feature separation according to noise types on both real and synthetic test datasets, where features from different noise categories are well-separated. In contrast, when the one-hot vectors in NIFM are incorrect (*i.e.*, mismatched with the image noise categories), the feature distributions generated by NIFM-based models are almost indistinguishable from those of models without NIFM, and the feature distributions of the two types of models exhibit a symmetric structure. This fully validates the effectiveness of using noise indicators to distinguish image noise types and using NIFM to fuse semantic features with noise indicators.

#### D. Ablation Studies

1) *Impact of Different Integration Schemes of NIFMs on Model Performance:* To deeply analyze the effectiveness of integration modes between the NIFM and the encoder, we construct two variants of NIFM integration strategies, as illustrated in Fig. 5. Fig. 5(a) presents the recursive integration strategy, where the output weight of the preceding NIFM is taken as one of the input features for the subsequent NIFM. Fig. 5(b) depicts the hybrid integration strategy, which

feeds the output weight of the previous NIFM as auxiliary features into the next NIFM based on the default integration mode. Meanwhile, we replace NIFM with a learnable prompt block [17] for training and testing. This alternative approach is also a popular learning scheme for noise type identification, as illustrated in Fig. 5(c). Subsequently, we retrained 21 models (combinations of 3 variant encoders and 7 decoders) using 100% of the training set, and the experimental results are shown in Table IV. It should be noted that the calculation method of the improvement ratio is the same as that in Table II. Due to space limitations, the results of Table II are not duplicated in Table IV.

As can be clearly observed from Table IV, across multiple groups of experiments on both the Synthesized test set and the Real test set, the recursive integration exhibits superior performance in most metrics. For instance, on the Synthesized test set, the average MAE of models under recursive integration is 0.0322 (+4.93%), while that under hybrid integration is 0.0326 (3.88%). In terms of metrics such as  $S$  and  $F_{\beta}^{adp}$ , the average improvement amplitude of recursive integration is also more significant. On the Real test set, the average MAE of recursive integration is 0.0205 (+14.21%), and that of hybrid integration is 0.0231 (+3.29%). This indicates that compared

TABLE IV  
COMPARISON OF MODEL PERFORMANCE USING TWO DISTINCT INTEGRATION STRATEGIES FOR NIFM. (A) DENOTES RECURSIVE FUSION, WHILE (B) REPRESENTS HYBRID FUSION.

Test set	Decoders	NIFM	$MAE \downarrow$		$S \uparrow$		$F_{\beta}^{adv} \uparrow$		$F_{\beta}^{mean} \uparrow$		$F_{\beta}^{max} \uparrow$		$E_{\xi}^{adv} \uparrow$		$E_{\xi}^{mean} \uparrow$		$E_{\xi}^{max} \uparrow$	
			val	$\Delta$	val	$\Delta$	val	$\Delta$	val	$\Delta$	val	$\Delta$	val	$\Delta$	val	$\Delta$	val	$\Delta$
Sys	F3Net	(a)	0.0307	13.03%	0.8845	1.25%	0.8322	2.60%	0.8411	2.23%	0.8587	1.82%	0.9239	1.15%	0.9200	1.19%	0.9309	1.05%
		(b)	0.0329	6.80%	0.8807	0.82%	0.8255	1.77%	0.8331	1.25%	0.8513	0.94%	0.9235	1.11%	0.9198	1.17%	0.9298	0.93%
		(c)	0.0388	-9.92%	0.8577	-1.82%	0.7999	-1.38%	0.8049	-2.17%	0.8243	-2.26%	0.9082	-0.57%	0.8986	-1.17%	0.9102	-1.20%
	MINET	(a)	0.0344	1.43%	0.8717	-0.04%	0.8153	-0.19%	0.8214	-0.06%	0.8407	-0.11%	0.9166	0.01%	0.9105	-0.06%	0.9193	-0.15%
		(b)	0.0357	-2.29%	0.8651	-0.80%	0.8196	0.34%	0.8234	0.18%	0.8370	-0.56%	0.9167	0.03%	0.9049	-0.67%	0.9176	-0.33%
		(c)	0.0375	-7.45%	0.8622	-1.13%	0.7973	-2.40%	0.8071	-1.81%	0.8289	-1.53%	0.9042	-1.34%	0.9037	-0.80%	0.9135	-0.78%
	EDN	(a)	0.0318	5.07%	0.8821	0.48%	0.8141	0.32%	0.8321	0.50%	0.8523	0.30%	0.9132	-0.07%	0.9140	0.62%	0.9272	0.49%
		(b)	0.0321	4.18%	0.8812	0.38%	0.8199	1.04%	0.8340	0.73%	0.8535	0.45%	0.9192	0.59%	0.9126	0.46%	0.9265	0.41%
		(c)	0.043	-28.36%	0.8418	-4.12%	0.7678	-5.37%	0.7756	-6.32%	0.7940	-6.55%	0.8906	-2.54%	0.8735	-3.85%	0.8928	-3.24%
	AESINet	(a)	0.0338	-3.05%	0.8672	-0.21%	0.8154	-1.21%	0.8209	-0.99%	0.8312	-0.64%	0.9150	-0.50%	0.9129	-0.12%	0.9169	-0.22%
		(b)	0.0336	-2.44%	0.8678	-0.15%	0.8141	-1.37%	0.8195	-1.17%	0.8315	-0.61%	0.9160	-0.40%	0.9131	-0.09%	0.9169	-0.22%
		(c)	0.0376	-14.63%	0.8497	-2.23%	0.8059	-2.37%	0.8070	-2.67%	0.8160	-2.46%	0.9050	-1.59%	0.8991	-1.63%	0.9039	-1.63%
	BAFSNet	(a)	0.0298	5.40%	0.8846	0.23%	0.8336	-0.13%	0.8438	0.41%	0.8618	0.67%	0.9286	0.07%	0.9249	0.54%	0.9342	0.45%
		(b)	0.0314	0.32%	0.8794	-0.35%	0.8317	-0.35%	0.8382	-0.26%	0.8542	-0.22%	0.9257	-0.25%	0.9173	-0.28%	0.9283	-0.18%
		(c)	0.0345	-9.52%	0.8711	-1.29%	0.8172	-2.10%	0.8231	-2.05%	0.8411	-1.75%	0.9176	-1.12%	0.9121	-0.85%	0.9213	-0.93%
	DC-Net	(a)	0.0281	12.46%	0.8915	1.00%	0.8464	1.47%	0.8516	1.40%	0.8653	1.11%	0.9328	0.55%	0.9248	0.44%	0.9347	0.27%
		(b)	0.0290	9.66%	0.8863	0.41%	0.8370	0.35%	0.8453	0.65%	0.8606	0.56%	0.9266	-0.12%	0.9210	0.03%	0.9299	-0.24%
		(c)	0.0326	-1.56%	0.8788	-0.44%	0.8360	0.23%	0.8391	-0.09%	0.8555	-0.04%	0.9246	-0.34%	0.9173	-0.37%	0.9262	-0.64%
	R-Net	(a)	0.0370	0.54%	0.8699	0.35%	0.8175	0.29%	0.8213	-0.10%	0.8370	-0.10%	0.9155	0.34%	0.9053	-0.17%	0.9188	0.27%
		(b)	0.0334	10.22%	0.8717	0.57%	0.8196	0.55%	0.8254	0.39%	0.8401	0.27%	0.9204	0.88%	0.9133	0.71%	0.9229	0.72%
		(c)	0.0551	-48.12%	0.8053	-7.09%	0.7355	-9.77%	0.7370	-10.36%	0.7504	-10.44%	0.8620	-5.52%	0.8510	-6.15%	0.8621	-5.92%
	Average	(a)	0.0322	4.93%	0.8788	0.44%	0.8249	0.45%	0.8332	0.48%	0.8496	0.44%	0.9208	0.22%	0.9161	0.35%	0.9260	0.31%
		(b)	0.0326	3.88%	0.8760	0.13%	0.8239	0.33%	0.8313	0.25%	0.8469	0.12%	0.9212	0.26%	0.9146	0.19%	0.9245	0.15%
		(c)	0.0399	-17.61%	0.8524	-2.58%	0.7942	-3.29%	0.7991	-3.62%	0.8157	-3.56%	0.9018	-1.85%	0.8936	-2.11%	0.9043	-2.04%
Real	F3Net	(a)	0.0239	3.63%	0.9020	0.43%	0.8262	1.49%	0.8467	1.09%	0.8825	2.23%	0.9219	0.80%	0.9257	0.65%	0.9425	0.87%
		(b)	0.0271	-9.27%	0.9008	0.29%	0.8230	1.09%	0.8423	0.57%	0.8795	1.87%	0.9209	0.69%	0.9230	0.35%	0.9402	0.62%
		(c)	0.0255	-2.82%	0.8947	-0.39%	0.8305	2.01%	0.8472	1.16%	0.8789	1.80%	0.9270	1.34%	0.9283	0.92%	0.9421	0.83%
	MINET	(a)	0.0206	11.21%	0.9127	1.33%	0.8471	2.45%	0.8675	2.42%	0.8983	1.61%	0.9398	1.19%	0.9424	1.53%	0.9529	0.61%
		(b)	0.0236	-1.72%	0.9084	0.85%	0.8373	1.25%	0.8613	1.68%	0.8863	0.26%	0.9284	0.56%	0.9336	0.58%	0.9445	-0.28%
		(c)	0.0225	3.02%	0.8997	-0.11%	0.8285	0.19%	0.8455	-0.18%	0.8872	0.36%	0.9240	0.08%	0.9294	0.13%	0.9465	-0.06%
	EDN	(a)	0.0211	5.38%	0.9069	-0.31%	0.8225	1.04%	0.8537	0.19%	0.8784	-0.73%	0.9245	0.95%	0.9311	0.41%	0.9419	-0.11%
		(b)	0.0227	-1.79%	0.9067	-0.32%	0.8130	-0.13%	0.8512	-0.09%	0.8828	-0.23%	0.9148	-0.11%	0.9284	0.13%	0.9439	0.10%
		(c)	0.0250	-12.11%	0.8868	-2.52%	0.7881	-3.18%	0.8208	-3.67%	0.8474	-4.23%	0.8960	-2.16%	0.9094	-1.93%	0.9259	-1.82%
	AESINet	(a)	0.0185	26.88%	0.9055	1.57%	0.8455	2.08%	0.8586	1.71%	0.8788	1.51%	0.9367	1.09%	0.9400	1.12%	0.9499	1.00%
		(b)	0.0281	-11.07%	0.8860	-0.63%	0.8125	-1.91%	0.8236	-2.43%	0.8436	-2.55%	0.9146	-1.29%	0.9160	-1.47%	0.9261	-1.16%
		(c)	0.0224	11.46%	0.8853	-0.71%	0.8354	0.85%	0.8374	-0.80%	0.8496	-1.87%	0.9261	-0.05%	0.9210	-0.93%	0.9256	-1.22%
	BAFSNet	(a)	0.0189	4.55%	0.9133	0.49%	0.8434	0.09%	0.8621	0.65%	0.8858	1.02%	0.9359	0.51%	0.9399	0.98%	0.9499	1.00%
		(b)	0.0201	-1.52%	0.9052	-0.40%	0.8330	-1.14%	0.8548	-0.20%	0.8818	0.57%	0.9262	-0.52%	0.9322	0.16%	0.9446	0.43%
		(c)	0.0200	-1.01%	0.9071	-0.19%	0.8462	0.02%	0.8600	0.40%	0.8898	1.48%	0.9425	1.22%	0.9429	1.31%	0.9545	1.49%
	DC-Net	(a)	0.0190	27.20%	0.9086	1.41%	0.8481	3.03%	0.8626	2.15%	0.8847	0.91%	0.9361	1.48%	0.9362	1.21%	0.9458	0.63%
		(b)	0.0211	19.16%	0.9086	1.41%	0.8377	1.76%	0.8616	2.03%	0.8862	1.08%	0.9282	0.63%	0.9358	1.17%	0.9470	0.75%
		(c)	0.0205	21.46%	0.9055	1.06%	0.8555	3.92%	0.8625	2.14%	0.8848	0.92%	0.9390	1.80%	0.9366	1.26%	0.9458	0.63%
	R-Net	(a)	0.0217	16.54%	0.9057	1.33%	0.8422	2.42%	0.8576	2.30%	0.8782	1.47%	0.9307	1.06%	0.9316	1.03%	0.9425	0.96%
		(b)	0.0193	25.77%	0.9105	1.86%	0.8481	3.14%	0.8629	2.94%	0.8855	2.30%	0.9386	1.92%	0.9387	1.80%	0.9499	1.76%
		(c)	0.0341	-31.15%	0.8570	-4.11%	0.7719	-6.13%	0.7834	-6.55%	0.8185	-5.43%	0.8904	-3.32%	0.8895	-3.52%	0.9058	-2.97%
	Average	(a)	0.0205	14.21%	0.9078	0.89%	0.8393	1.80%	0.8584	1.50%	0.8838	1.14%	0.9322	1.10%	0.9353	0.99%	0.9465	0.76%
		(b)	0.0231	3.28%	0.9037	0.43%	0.8292	0.57%	0.8511	0.64%	0.8780	0.47%	0.9246	0.26%	0.9297	0.39%	0.9423	0.32%
		(c)	0.0243	-1.49%	0.8909	-0.99%	0.8223	-0.27%	0.8367	-1.07%	0.8652	-0.99%	0.9207	-0.15%	0.9224	-0.39%	0.9352	-0.45%

with the hybrid integration strategy, the recursive integration strategy can transfer and fuse noise indication information more efficiently.

However, the performance gains generated by these two variants are both lower than that of the default integration strategy. Taking the average MAE as an example, the gain ratios of the default integration strategy on the synthetic test set and the real test set are 7.27% and 17.67%, respectively, which far exceed those of the recursive integration strategy (4.93% and 14.21%) and the hybrid integration strategy (3.88% and 3.28%). The aforementioned experimental results verify the crucial role of reasonably designing the integration mode of NIFM in improving the segmentation performance of the model under complex weather conditions.

Furthermore, models incorporating the prompt block exhibit decreased average performance on both synthesized and Real test set. We attribute this phenomenon primarily to the fact that optimizing the learnable prompt relies on sufficiently large datasets. Massive data is crucial for boosting model learning of noise specific representations.

2) *The Effectiveness of NIFM Meeting Various Backbone Networks*: To evaluate the compatibility of NIFM with dif-

ferent backbone networks, we replace the ResNet-50 in the framework with MobileNet [95] and MobileViT [96]. As presented in Table V, on the real test set, the introduction of NIFM into the MobileNet and MobileViT backbones improved the average MAE across seven models by 14.78% and 4.96%, respectively, demonstrating the compatibility of NIFM with diverse backbone networks. On the other hand, the performance gains brought by NIFM are more pronounced in ResNet and MobileNet settings compared to MobileViT. This phenomenon can be attributed to the superior feature extraction capability of Transformer-based architectures, which partially diminishes the contribution of noise-type guidance mechanisms.

3) *Impact of Training Data Diversity on Model Performance*: To verify that training models with images containing various weather noises yields better robustness than training with clean images or images with a single noise type serves as a prerequisite for this study on leveraging noise characteristics to enhance model segmentation performance under complex weather conditions. Thus, seven models (each composed of the conventional ResNet-50 and decoder) are trained using different training subsets. The experimental results are pre-

TABLE V  
COMPARISON OF MODEL PERFORMANCE USING DIFFERENT BACKBONES, NAMELY MOBILENET AND MOBILEViT.

Test set	Decoder	NIFM	MobileNet								MobileViT							
			MAE $\downarrow$		$S \uparrow$		$F_{\beta}^{mean} \uparrow$		$E_{\xi}^{mean} \uparrow$		MAE $\downarrow$		$S \uparrow$		$F_{\beta}^{mean} \uparrow$		$E_{\xi}^{mean} \uparrow$	
			val	$\Delta$	val	$\Delta$	val	$\Delta$	val	$\Delta$	val	$\Delta$	val	$\Delta$	val	$\Delta$	val	$\Delta$
Sys	F3Net	✓	0.0583		0.8011		0.7216		0.8455		0.0447		0.8445		0.7839		0.8874	
		✓	0.0579	0.69%	0.8035	0.30%	0.7261	0.62%	0.8462	0.08%	0.0424	5.15%	0.8498	0.62%	0.7935	1.23%	0.8943	0.78%
	MINET	✓	0.0368		0.8679		0.8154		0.9058		0.0462		0.8350		0.7745		0.8751	
		✓	0.0333	9.51%	0.8748	0.79%	0.8282	1.57%	0.9119	0.67%	0.0466	-0.87%	0.8370	0.24%	0.7769	0.30%	0.8799	0.55%
	EDN	✓	0.0376		0.8637		0.8039		0.8958		0.0475		0.8379		0.7647		0.8688	
		✓	0.0341	9.31%	0.8710	0.84%	0.8160	1.51%	0.9052	1.05%	0.0457	3.79%	0.8410	0.36%	0.7717	0.91%	0.8716	0.33%
	AESINet	✓	0.0342		0.8526		0.8050		0.8957		0.0478		0.8197		0.7526		0.8761	
		✓	0.0354	-3.51%	0.8604	0.91%	0.8152	1.27%	0.9049	1.03%	0.0484	-1.26%	0.8219	0.27%	0.7608	1.09%	0.8738	-0.26%
	BAFSNet	✓	0.0315		0.8829		0.8358		0.9193		0.0416		0.8453		0.7870		0.8869	
		✓	0.0322	-2.22%	0.8823	-0.07%	0.8360	0.01%	0.9177	-0.17%	0.0426	-2.40%	0.8439	-0.17%	0.7873	0.04%	0.8885	0.18%
Real	DC-Net	✓	0.0354		0.8682		0.8225		0.9066		0.0388		0.8600		0.8036		0.8995	
		✓	0.0331	6.50%	0.8771	1.03%	0.8276	0.61%	0.9160	1.04%	0.0414	-6.70%	0.8462	-1.60%	0.7884	-1.89%	0.8899	-1.06%
	R-Net	✓	0.0509		0.8112		0.7469		0.8585		0.0637		0.7643		0.6787		0.8023	
		✓	0.0506	0.59%	0.8217	1.30%	0.7593	1.66%	0.8632	0.55%	0.0604	5.18%	0.7904	3.42%	0.7143	5.24%	0.8340	3.96%
	Average	✓	0.0407		0.8497		0.7930		0.8896		0.0479		0.8287		0.7611		0.8702	
		✓	0.0395	2.85%	0.8558	0.73%	0.8012	1.03%	0.8950	0.61%	0.0486	-1.49%	0.8275	-0.14%	0.7612	0.02%	0.8709	0.09%
	F3Net	✓	0.0411		0.8344		0.7464		0.8623		0.0324		0.8754		0.8115		0.9063	
		✓	0.0373	9.25%	0.8388	0.53%	0.7527	0.84%	0.8587	-0.41%	0.0272	16.05%	0.8884	1.48%	0.8332	2.67%	0.9166	1.13%
	MINET	✓	0.0264		0.8972		0.8455		0.9226		0.0296		0.8787		0.8200		0.9051	
		✓	0.0227	14.02%	0.9037	0.73%	0.8501	0.54%	0.9247	0.23%	0.0279	5.74%	0.8846	0.68%	0.8190	-0.13%	0.9166	1.27%
Real	EDN	✓	0.0357		0.8810		0.8108		0.8972		0.0327		0.8680		0.7954		0.8922	
		✓	0.0229	35.85%	0.9029	2.48%	0.8382	3.38%	0.9207	2.63%	0.0291	11.01%	0.8749	0.80%	0.8103	1.86%	0.9015	1.05%
	AESINet	✓	0.0273		0.8753		0.8170		0.9051		0.0272		0.8683		0.7997		0.9120	
		✓	0.0240	12.09%	0.8980	2.58%	0.8457	3.52%	0.9303	2.78%	0.0267	1.84%	0.8753	0.81%	0.8166	2.11%	0.9140	0.21%
	BAFSNet	✓	0.0242		0.8983		0.8366		0.9217		0.0275		0.8795		0.8201		0.9174	
		✓	0.0213	11.98%	0.9076	1.03%	0.8541	2.09%	0.9316	1.07%	0.0251	8.73%	0.8910	1.30%	0.8352	1.84%	0.9226	0.57%
	DC-Net	✓	0.0264		0.8954		0.8401		0.9246		0.0250		0.8860		0.8263		0.9221	
		✓	0.0225	14.77%	0.9054	1.11%	0.8426	0.30%	0.9262	0.18%	0.0256	-2.40%	0.8828	-0.36%	0.8294	0.38%	0.9183	-0.41%
	R-Net	✓	0.0334		0.8662		0.7998		0.8947		0.0438		0.8199		0.7431		0.8470	
		✓	0.0321	3.89%	0.8651	-0.13%	0.7965	-0.40%	0.8880	-0.75%	0.0337	23.06%	0.8513	3.83%	0.7837	5.47%	0.8847	4.46%
Real	Average	✓	0.0306		0.8783		0.8138		0.9040		0.0322		0.8644		0.7956		0.8969	
		✓	0.0261	14.78%	0.8888	1.20%	0.8257	1.47%	0.9115	0.82%	0.0306	4.96%	0.8667	0.26%	0.8001	0.56%	0.8965	-0.03%

sented in Table VI, where the second-to-last row “Multi-weather” indicates that the seven methods are trained using the complete WXSOD training set (100% training data), and the last row “Multi-weather (w.NIFM)” denotes that the seven methods further adopt the specific encoder enhanced by NIFM. Due to space limitations, we will subsequently focus analysis primarily on the average results.

From Table VI, it can be observed that models trained with the larger-scale and noise-diverse mixed training set (*i.e.*, “Multi-weather”) can significantly improve segmentation performance, with all evaluation metrics enhanced. On the other hand, models trained on subsets with a single noise type (*e.g.*, “Dark”, “Fog” and “Snow&Fog”) generally perform worse in all metrics compared to those trained on the “Clean” subset. This is mainly because the test set contains complex noise types, and using a training set with a single noise type instead enlarges the domain gap between training and test data, undermining the model’s generalization ability. Secondly, in terms of various evaluation metrics of both the Synthesized test set and the Real test set, the model represented by “Multi-weather (w.NIFM)” performs significantly better than the model corresponding to “Multi-weather”. Taking the average MAE metric as an example, on the Synthesized test set, the average MAE of “Multi-weather (w.NIFM)” is 0.0315, which is lower than 0.0339 of “Multi-weather”; on the Real test set, the average MAE of the former is 0.0197, also significantly lower than 0.0239 of the latter. For other metrics such as  $S$  and  $F_{\beta}^{adv}$ , “Multi-weather (w.NIFM)”-based models also achieves the optimal results of most key metrics. This demonstrates that enhancing the specific encoder via NIFM can effectively integrate multi-type weather noise information and significantly

improve the model’s segmentation performance for salient objects in complex weather scenarios, further verifying the effectiveness of the method proposed in this paper in utilizing noise differences.

We also provide visual comparisons of the BAFSNet model under different training subset settings, as shown in Fig. 7 and Fig. 8. In contrast to training subsets with a single noise type, BAFSNet, when trained under the “Multi-weather” setting with richer training data, exhibits more precise segmentation results. Moreover, upon integrating NIFM into the conventional encoder utilized in BAFSNet based on the “Multi-weather” setup, the segmentation accuracy is further improved.

## V. CONCLUSION

This paper focuses on the SOD under complex weather-corrupted scenarios, which represents a practical yet understudied task. Most existing SOD methods are designed under the clean-image assumption, and their performance tends to degrade under adverse weather conditions. To address this limitation, we propose a SOD framework consisting of a weather-aware encoder and a replaceable decoder, which can be seamlessly integrated with other SOD models. The core of this work lies in a novel Noise Indicator Fusion Module (NIFM). NIFM takes both semantic features and a one-hot noise indicator as inputs to adaptively learn noise-type-dependent feature weights, thereby performing secondary modulation on the semantic features extracted by the encoder. To ensure comprehensive feature refinement, we embed one NIFM between every two consecutive stages of the encoder, enabling progressive modulation of multi-scale semantic features. Extensive experiments are conducted on the WXSOD

TABLE VI  
QUANTITATIVE COMPARISON RESULTS OF  $MAE$ ,  $S$ ,  $F_{\beta}^{mean}$  AND  $E_{\xi}^{mean}$  ON THE WXSOD DATASET. HERE, " $\uparrow$ " ( $\downarrow$ ) MEANS THAT THE LARGER (SMALLER) THE BETTER. THE "SYS" AND "REAL" DENOTES THE SYNTHESIZED AND REAL TEST SET, RESPECTIVELY. THE BEST RESULTS ARE HIGHLIGHTED IN **BOLD**.

Test set	Method	Metrics	Training subset										
			Clean	Rain	Snow	Fog	Light	Dark	Rain&Fog	Rain&Snow	Snow&Fog	Multi-weather	Multi-weather (w.NIFM)
Sys	F3Net	MAE↓	0.0701	0.0676	0.0570	0.0796	0.0697	0.0817	0.0887	0.0606	0.1200	0.0353	0.0307
		S↑	0.7396	0.7429	0.7914	0.7124	0.7337	0.7208	0.6403	0.7837	0.6633	0.8735	0.8822
		F <sub>β</sub> <sup>mean</sup> ↑	0.6146	0.6163	0.7080	0.5586	0.6004	0.5834	0.4265	0.6883	0.4926	0.8228	0.8422
		E <sub>ξ</sub> <sup>mean</sup> ↑	0.7428	0.7295	0.8091	0.6852	0.7197	0.7185	0.5979	0.8019	0.6574	0.9092	0.9210
	MINET	MAE↓	0.0726	0.0680	0.0627	0.1113	0.0764	0.0742	0.0871	0.0681	0.0752	0.0349	0.0324
		S↑	0.7500	0.7407	0.7881	0.7415	0.7398	0.7457	0.7095	0.7693	0.7572	0.8721	0.8772
		F <sub>β</sub> <sup>mean</sup> ↑	0.6525	0.6377	0.7021	0.6347	0.6261	0.6388	0.5561	0.6865	0.6610	0.8219	0.8273
		E <sub>ξ</sub> <sup>mean</sup> ↑	0.7764	0.7535	0.8095	0.7676	0.7827	0.7586	0.7134	0.8011	0.7999	0.9110	0.9140
	EDN	MAE↓	0.0573	0.0534	0.0497	0.0558	0.0614	0.0550	0.0630	0.0481	0.0553	0.0335	0.0317
		S↑	0.7719	0.8021	0.8213	0.7814	0.7606	0.7960	0.7796	0.8296	0.8015	0.8779	0.8827
		F <sub>β</sub> <sup>mean</sup> ↑	0.6829	0.7220	0.7541	0.6864	0.6491	0.7095	0.6745	0.7618	0.7136	0.8280	0.8337
		E <sub>ξ</sub> <sup>mean</sup> ↑	0.7798	0.8181	0.8472	0.7861	0.7624	0.8243	0.7950	0.8613	0.8188	0.9084	0.9145
	AESINet	MAE↓	0.0668	0.0617	0.0555	0.0702	0.0616	0.0663	0.0811	0.0606	0.0904	0.0328	0.0314
		S↑	0.7268	0.7388	0.7920	0.7352	0.7430	0.7140	0.6744	0.7607	0.7027	0.8691	0.8714
		F <sub>β</sub> <sup>mean</sup> ↑	0.7325	0.6284	0.7065	0.6322	0.6343	0.5796	0.4997	0.6690	0.5768	0.8292	0.8306
		E <sub>ξ</sub> <sup>mean</sup> ↑	0.7325	0.7438	0.8298	0.7687	0.7827	0.7054	0.6570	0.7842	0.7159	0.9140	0.9160
	BAFSNet	MAE↓	0.0620	0.0583	0.0501	0.0732	0.0611	0.0669	0.0711	0.0511	0.0770	0.0315	0.0298
		S↑	0.7444	0.7692	0.8183	0.7321	0.7620	0.7444	0.7206	0.8151	0.6784	0.8825	0.8857
		F <sub>β</sub> <sup>mean</sup> ↑	0.6448	0.6791	0.7588	0.6132	0.6577	0.6305	0.5835	0.7468	0.5322	0.8404	0.8422
		E <sub>ξ</sub> <sup>mean</sup> ↑	0.7428	0.7786	0.8511	0.7413	0.7814	0.7510	0.7341	0.8485	0.6644	0.9199	0.9273
	DC-Net	MAE↓	0.0753	0.0698	0.0747	0.0732	0.0779	0.0773	0.0808	0.0573	0.0749	0.0321	0.0315
		S↑	0.7010	0.7565	0.7624	0.7311	0.7168	0.7263	0.7325	0.7980	0.7577	0.8827	0.8817
		F <sub>β</sub> <sup>mean</sup> ↑	0.5550	0.6553	0.6694	0.6116	0.5838	0.6050	0.6049	0.7197	0.6603	0.8399	0.8382
		E <sub>ξ</sub> <sup>mean</sup> ↑	0.6834	0.7663	0.7878	0.7386	0.7144	0.7466	0.7404	0.8300	0.7746	0.9207	0.9153
	RNet	MAE↓	0.0614	0.0632	0.0574	0.0714	0.0687	0.0673	0.0815	0.0606	0.0893	0.0372	0.0329
		S↑	0.7471	0.7544	0.7898	0.7371	0.7117	0.7435	0.6766	0.7768	0.6738	0.8668	0.8762
		F <sub>β</sub> <sup>mean</sup> ↑	0.6412	0.6338	0.7075	0.6094	0.5703	0.6109	0.4930	0.6848	0.5208	0.8221	0.8313
		E <sub>ξ</sub> <sup>mean</sup> ↑	0.7567	0.7575	0.8011	0.7297	0.6922	0.7408	0.6386	0.7991	0.6689	0.9068	0.9144
	Average	MAE↓	0.0665	0.0631	0.0582	0.0764	0.0681	0.0698	0.0790	0.0581	0.0832	0.0339	0.0315
		S↑	0.7401	0.7578	0.7948	0.7387	0.7382	0.7415	0.7048	0.7905	0.7192	0.8749	0.8796
		F <sub>β</sub> <sup>mean</sup> ↑	0.6309	0.6532	0.7152	0.6209	0.6174	0.6225	0.5483	0.7081	0.5939	0.8292	0.8351
		E <sub>ξ</sub> <sup>mean</sup> ↑	0.7449	0.7639	0.8194	0.7453	0.7479	0.7493	0.6966	0.8180	0.7286	0.9129	0.9175
Real	F3Net	MAE↓	0.0346	0.0490	0.0372	0.1494	0.0351	0.0469	0.0827	0.0476	0.1493	0.0248	0.0196
		S↑	0.8481	0.8006	0.8332	0.7559	0.8468	0.8305	0.6354	0.7963	0.5801	0.8982	0.9133
		F <sub>β</sub> <sup>mean</sup> ↑	0.7630	0.6853	0.7384	0.6776	0.7663	0.7384	0.3958	0.6796	0.3416	0.8375	0.8611
		E <sub>ξ</sub> <sup>mean</sup> ↑	0.8563	0.7876	0.8386	0.7722	0.8606	0.8462	0.5663	0.7870	0.5444	0.9198	0.9383
	MINET	MAE↓	0.0373	0.0496	0.0366	0.0601	0.0449	0.0355	0.0903	0.0514	0.1130	0.0232	0.0241
		S↑	0.8652	0.8003	0.8527	0.8330	0.8451	0.8559	0.7073	0.8046	0.7316	0.9007	0.9038
		F <sub>β</sub> <sup>mean</sup> ↑	0.7942	0.7076	0.7823	0.7394	0.7686	0.7721	0.5218	0.7010	0.6055	0.8470	0.8445
		E <sub>ξ</sub> <sup>mean</sup> ↑	0.8928	0.8063	0.8683	0.8529	0.8787	0.8849	0.7116	0.8087	0.7545	0.9282	0.9250
	EDN	MAE↓	0.0295	0.0301	0.0240	0.0261	0.0278	0.0312	0.0422	0.0337	0.0454	0.0223	0.0183
		S↑	0.8857	0.8887	0.8921	0.8931	0.8653	0.8878	0.8244	0.8717	0.8377	0.9097	0.9173
		F <sub>β</sub> <sup>mean</sup> ↑	0.8170	0.8178	0.8197	0.8200	0.7820	0.8188	0.7097	0.7942	0.7432	0.8520	0.8634
		E <sub>ξ</sub> <sup>mean</sup> ↑	0.8993	0.9083	0.9111	0.9088	0.8818	0.9120	0.8261	0.8875	0.8514	0.9272	0.9395
	AESINet	MAE↓	0.0368	0.0387	0.0389	0.0785	0.0323	0.0393	0.1011	0.0478	0.2105	0.0253	0.0179
		S↑	0.8459	0.8071	0.8556	0.8004	0.8616	0.8213	0.6912	0.7921	0.6237	0.8916	0.9097
		F <sub>β</sub> <sup>mean</sup> ↑	0.7750	0.7095	0.7710	0.7049	0.8015	0.7352	0.5422	0.6900	0.5163	0.8441	0.8694
		E <sub>ξ</sub> <sup>mean</sup> ↑	0.8689	0.8160	0.8841	0.8271	0.8953	0.8429	0.6977	0.8042	0.6293	0.9297	0.9441
	BAFSNet	MAE↓	0.0300	0.0355	0.0278	0.1199	0.0339	0.0354	0.0649	0.0339	0.0765	0.0198	0.0197
		S↑	0.8726	0.8339	0.8870	0.7609	0.8631	0.8685	0.7154	0.8546	0.6545	0.9088	0.9132
		F <sub>β</sub> <sup>mean</sup> ↑	0.8139	0.7575	0.8339	0.6559	0.7910	0.7924	0.5490	0.7776	0.4459	0.8565	0.8620
		E <sub>ξ</sub> <sup>mean</sup> ↑	0.8978	0.8530	0.9206	0.7805	0.8899	0.8939	0.6971	0.8786	0.6062	0.9307	0.9395
	DC-Net	MAE↓	0.0399	0.0451	0.0538	0.0458	0.0440	0.0411	0.1174	0.0483	0.0693	0.0261	0.0194
		S↑	0.8481	0.8214	0.8084	0.8503	0.8307	0.8372	0.7422	0.8242	0.7786	0.8960	0.9079
		F <sub>β</sub> <sup>mean</sup> ↑	0.7675	0.7225	0.7169	0.7747	0.7380	0.7524	0.6228	0.7237	0.6724	0.8444	0.8611
		E <sub>ξ</sub> <sup>mean</sup> ↑	0.8686	0.8297	0.8251	0.8635	0.8505	0.8550	0.7455	0.8277	0.7904	0.9249	0.9356
	R-Net	MAE↓	0.0380	0.0450	0.0305	0.0545	0.0385	0.0458	0.0719	0.0452	0.1044	0.0260	0.0189
		S↑	0.8581	0.8103	0.8763	0.8225	0.7968	0.8629	0.7116	0.8014	0.6537	0.8938	0.9150
		F <sub>β</sub> <sup>mean</sup> ↑	0.7827	0.6971	0.8165	0.7191	0.6750	0.7866	0.5377	0.6830	0.4582	0.8383	0.8663
		E <sub>ξ</sub> <sup>mean</sup> ↑	0.8792	0.8051	0.8921	0.8344	0.7901	0.8877	0.6758	0.7937	0.6250	0.9220	0.9434
	Average	MAE↓	0.0352	0.0419	0.0355	0.0763	0.0366	0.0393	0.0815	0.0440	0.1098	0.0239	0.0197
		S↑	0.8605	0.8232	0.8579	0.8166	0.8442	0.8520	0.7182	0.8207	0.6943	0.8998	0.9114
		F <sub>β</sub> <sup>mean</sup> ↑	0.7876	0.7282	0.7827	0.7274	0.7604	0.7708	0.5541	0.7213	0.5404	0.8457	0.8611
		E <sub>ξ</sub> <sup>mean</sup> ↑	0.8804	0.8294	0.8771	0.8342	0.8638	0.8747	0.7029	0.8268	0.6859	0.9261	0.9379

dataset, covering multiple training data scales (100%, 50%, and 30% of the full training set) and seven distinct decoder configurations. Results demonstrate that, compared with conventional encoders, the NIFM-enhanced encoder achieves improved detection accuracy under complex weather conditions. Future work will explore extending the noise indicator to more continuous or implicit representations, and validate the

framework's effectiveness on a wider ranger of unstructured degradations.

## REFERENCES

- [1] Y. Zhuge, Y. Zeng, and H. Lu, "Deep embedding features for salient object detection," ser. Proceedings of the AAAI Conference on Artificial Intelligence, 2019, pp. 9340–9347.

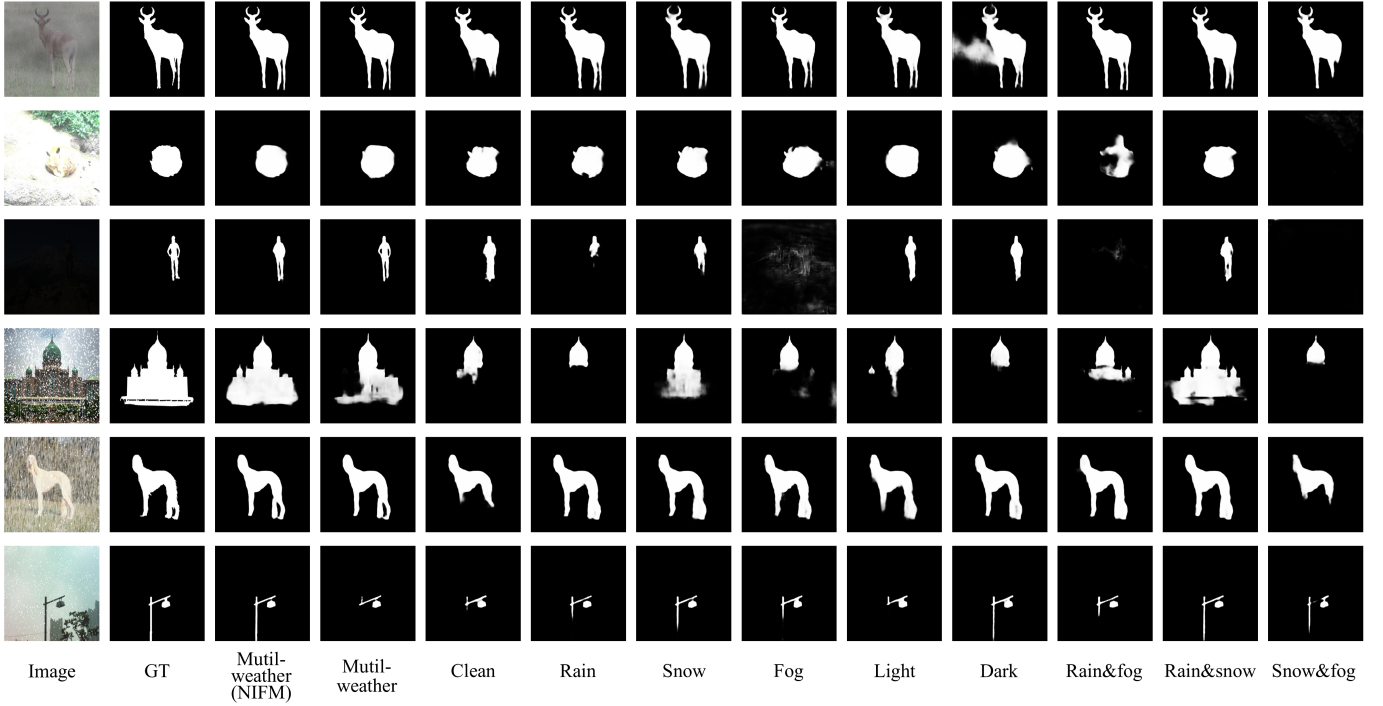


Fig. 7. Visual Comparison on synthesized test set across different training subsets.

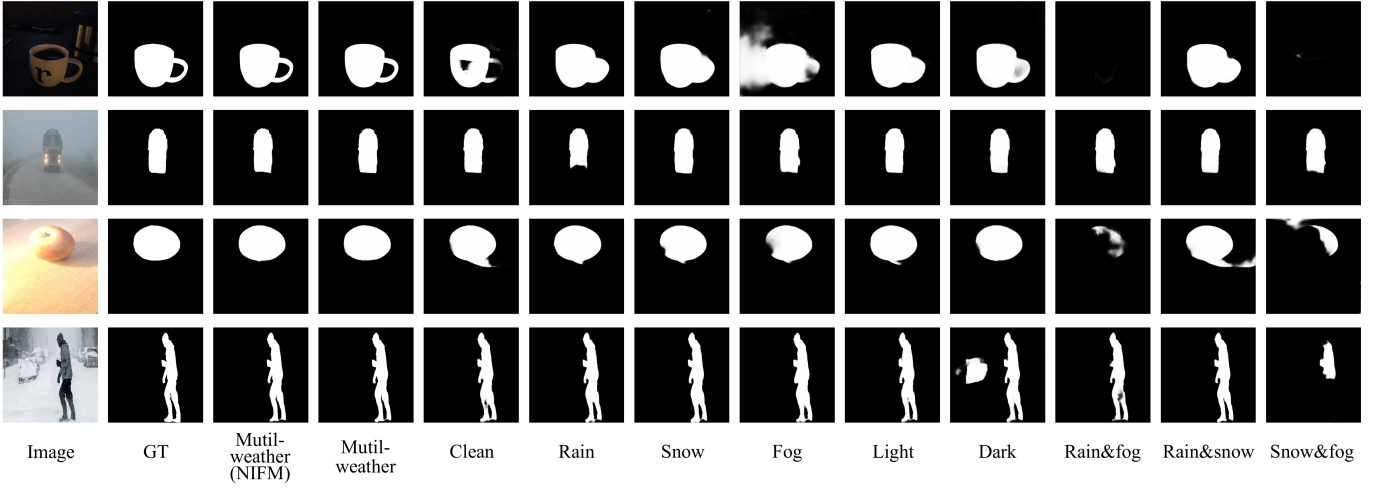


Fig. 8. Visual Comparison on real test set across different training subsets.

- [2] Y. Wang, R. Wang, X. Fan, T. Wang, and X. He, "Pixels, regions, and objects: Multiple enhancement for salient object detection," ser. Proceedings of the IEEE/CVF conference on computer vision and pattern recognition, 2023, pp. 10 031–10 040.
- [3] J. Jin, Q. Jiang, Q. Wu, B. Xu, and R. Cong, "Underwater salient object detection via dual-stage self-paced learning and depth emphasis," *IEEE Transactions on Circuits and Systems for Video Technology*, 2024.
- [4] X. Song, P. Zhang, X. Lu, X. Hei, and R. Liu, "A universal multi-view guided network for salient object and camouflaged object detection," *IEEE Transactions on Circuits and Systems for Video Technology*, vol. 34, no. 11, pp. 11 184–11 197, 2024.
- [5] Q. Zhang, S. Wang, X. Wang, Z. Sun, S. Kwong, and J. Jiang, "A multi-task collaborative network for light field salient object detection," *IEEE Transactions on Circuits and Systems for Video Technology*, vol. 31, no. 5, pp. 1849–1861, 2020.
- [6] J. He, K. Fu, X. Liu, and Q. Zhao, "Samba: A unified mamba-based framework for general salient object detection," in *Proceedings of the Computer Vision and Pattern Recognition Conference*, 2025, pp. 25 314–25 324.
- [7] J. Wang, K. Song, Y. Bao, L. Huang, and Y. Yan, "Cgfnnet: Cross-guided fusion network for rgb-t salient object detection," *IEEE Transactions on Circuits and Systems for Video Technology*, vol. 32, no. 5, pp. 2949–2961, 2021.
- [8] Z. Liu, Y. Tan, Q. He, and Y. Xiao, "Swinnet: Swin transformer drives edge-aware rgb-d and rgb-t salient object detection," *IEEE Transactions on Circuits and Systems for Video Technology*, vol. 32, no. 7, pp. 4486–4497, 2021.
- [9] W. Zhou, F. Sun, Q. Jiang, R. Cong, and J.-N. Hwang, "Wavenet: Wavelet network with knowledge distillation for rgb-t salient object detection," *IEEE Transactions on Image Processing*, vol. 32, pp. 3027–3039, 2023.
- [10] G. Chen, F. Shao, X. Chai, H. Chen, Q. Jiang, X. Meng, and Y.-S. Ho, "Modality-induced transfer-fusion network for rgb-d and rgb-t salient object detection," *IEEE Transactions on Circuits and Systems for Video Technology*, vol. 33, no. 4, pp. 1787–1801, 2022.
- [11] X. Zhang, Y. Xu, T. Wang, and T. Liao, "Multi-prior driven network

- for rgb-d salient object detection,” *IEEE Transactions on Circuits and Systems for Video Technology*, vol. 34, no. 10, pp. 9209–9222, 2023.
- [12] Y. Wang, L. Zhang, P. Zhang, Y. Zhuge, J. Wu, H. Yu, and H. Lu, “Learning local-global representation for scribble-based rgb-d salient object detection via transformer,” *IEEE Transactions on Circuits and Systems for Video Technology*, 2024.
  - [13] B. Wan, X. Zhou, Y. Sun, T. Wang, C. Lv, S. Wang, H. Yin, and C. Yan, “Mffnet: Multi-modal feature fusion network for vdt salient object detection,” *IEEE Transactions on Multimedia*, vol. 26, pp. 2069–2081, 2023.
  - [14] Y. Luo, F. Shao, B. Mu, H. Chen, Z. Li, and Q. Jiang, “Dynamic weighted fusion and progressive refinement network for visible-depth-thermal salient object detection,” *IEEE Transactions on Circuits and Systems for Video Technology*, vol. 34, no. 11, pp. 10 662–10 677, 2024.
  - [15] L. Bao, X. Zhou, B. Zheng, R. Cong, H. Yin, J. Zhang, and C. Yan, “Ifenet: Interaction, fusion, and enhancement network for vdt salient object detection,” *IEEE Transactions on Image Processing*, 2025.
  - [16] B. Li, X. Liu, P. Hu, Z. Wu, J. Lv, and X. Peng, “All-in-one image restoration for unknown corruption,” ser. Proceedings of the IEEE/CVF conference on computer vision and pattern recognition, 2022, pp. 17 452–17 462.
  - [17] V. Potlapalli, S. W. Zamir, S. H. Khan, and F. Shahbaz Khan, “Promptir: Prompting for all-in-one image restoration,” pp. 71 275–71 293, 2023.
  - [18] Y. Jiang, Z. Zhang, T. Xue, and J. Gu, “Autodir: Automatic all-in-one image restoration with latent diffusion,” ser. European Conference on Computer Vision. Springer, 2024, pp. 340–359.
  - [19] T. Wang, Z. Zheng, Y. Sun, C. Yan, Y. Yang, and T.-S. Chua, “Multiple-environment self-adaptive network for aerial-view geo-localization,” *Pattern Recognition*, vol. 152, p. 110363, 2024.
  - [20] T. Feng, Q. Li, X. Wang, M. Wang, G. Li, and W. Zhu, “Multi-weather cross-view geo-localization using denoising diffusion models,” ser. Proceedings of the 2nd Workshop on UAVs in Multimedia: Capturing the World from a New Perspective, 2024, pp. 35–39.
  - [21] J. Wen, H. Yu, and Z. Zheng, “Weatherprompt: Multi-modality representation learning for all-weather drone visual geo-localization,” *arXiv preprint arXiv:2508.09560*, 2025.
  - [22] H. Jiang, J. Wang, Z. Yuan, Y. Wu, N. Zheng, and S. Li, “Salient object detection: A discriminative regional feature integration approach,” ser. Proceedings of the IEEE conference on computer vision and pattern recognition, 2013, pp. 2083–2090.
  - [23] J. Kim, D. Han, Y.-W. Tai, and J. Kim, “Salient region detection via high-dimensional color transform and local spatial support,” *IEEE transactions on image processing*, vol. 25, no. 1, pp. 9–23, 2015.
  - [24] H. Yu, H. Zhang, Z. Zhang, and S. Yang, “State estimation of lithium-ion batteries via physics-machine learning combined methods: A methodological review and future perspectives,” *ETransportation*, p. 100420, 2025.
  - [25] Q. Chen, T. Wang, Z. Yang, H. Li, R. Lu, Y. Sun, B. Zheng, and C. Yan, “Sdpl: Shifting-dense partition learning for uav-view geo-localization,” *IEEE Transactions on Circuits and Systems for Video Technology*, vol. 34, no. 11, pp. 11 810–11 824, 2024.
  - [26] Q. Chen, T. Wang, R. Lu, Y. Liu, B. Zheng, and Z. Zheng, “Scale-adaptive uav geo-localization via height-aware partition learning,” *arXiv preprint arXiv:2412.11535*, 2024.
  - [27] T. Feng, X. Wang, F. Han, L. Zhang, and W. Zhu, “U2udata: A large-scale cooperative perception dataset for swarm uavs autonomous flight,” ser. Proceedings of the 32nd ACM International Conference on Multimedia, 2024, pp. 7600–7608.
  - [28] T. Feng, X. Wang, Z. Zhou, R. Wang, Y. Zhan, G. Li, Q. Li, and W. Zhu, “Evoagent: Agent autonomous evolution with continual world model for long-horizon tasks,” *arXiv preprint arXiv:2502.05907*, 2025.
  - [29] T. Feng, X. Wang, Y.-G. Jiang, and W. Zhu, “Embodied ai: From llms to world models,” in *IEEE Circuits and Systems Magazine*, 2025.
  - [30] X. Yu, C. Wang, H. Jin, A. Elazab, G. Jia, X. Wan, C. Zou, and R. Ge, “Crisp-sam2: Sam2 with cross-modal interaction and semantic prompting for multi-organ segmentation,” *arXiv preprint arXiv:2506.23121*, 2025.
  - [31] X. Yu, Z. Chen, Y. Zhang, S. Lu, R. Shen, J. Zhang, X. Hu, Y. Fu, and S. Yan, “Visual document understanding and question answering: A multi-agent collaboration framework with test-time scaling,” *arXiv preprint arXiv:2508.03404*, 2025.
  - [32] W. Shi, Y. Pan, C. Zhao, Y. Liu, S. Zhang, H. Zhang, and Y. Wen, “Multi-scale transformer for image restoration,” *CAAI Transactions on Intelligence Technology*, 2025.
  - [33] S. He, J. Shen, H. Yang, G. Xu, and L. T. Yang, “A temporal correlation networks based on interactive modelling for remote sensing images change detection,” *CAAI Transactions on Intelligence Technology*, 2025.
  - [34] S. Liu, C. Luo, K. Yan, F. Qin, R. Ge, Y. Peng, J. Huang, N. Zheng, Y. Zhang, and C. Wang, “La-yolo: Location refinement and adjacent feature fusion-based infrared small target detection,” *CAAI Transactions on Intelligence Technology*, 2025.
  - [35] Z. Guo, D. Wu, C. Gao, and N. Sang, “Selective multiple classifiers for weakly supervised semantic segmentation,” *CAAI Transactions on Intelligence Technology*, 2025.
  - [36] S. Chen, X. Tan, B. Wang, and X. Hu, “Reverse attention for salient object detection,” ser. Proceedings of the European conference on computer vision (ECCV), 2018, pp. 234–250.
  - [37] Y. Pang, X. Zhao, L. Zhang, and H. Lu, “Multi-scale interactive network for salient object detection,” ser. Proceedings of the IEEE/CVF conference on computer vision and pattern recognition, 2020, pp. 9413–9422.
  - [38] Z. Wang, J. Guo, C. Zhang, and B. Wang, “Multiscale feature enhancement network for salient object detection in optical remote sensing images,” *IEEE Transactions on Geoscience and Remote Sensing*, vol. 60, pp. 1–19, 2022.
  - [39] C. Yang, L. Zhang, H. Lu, X. Ruan, and M.-H. Yang, “Saliency detection via graph-based manifold ranking,” ser. Proceedings of the IEEE conference on computer vision and pattern recognition, 2013, pp. 3166–3173.
  - [40] J. Shi, Q. Yan, L. Xu, and J. Jia, “Hierarchical image saliency detection on extended cssd,” *IEEE transactions on pattern analysis and machine intelligence*, vol. 38, no. 4, pp. 717–729, 2015.
  - [41] L. Wang, H. Lu, Y. Wang, M. Feng, D. Wang, B. Yin, and X. Ruan, “Learning to detect salient objects with image-level supervision,” ser. Proceedings of the IEEE conference on computer vision and pattern recognition, 2017, pp. 136–145.
  - [42] X. Deng, P. Zhang, W. Liu, and H. Lu, “Recurrent multi-scale transformer for high-resolution salient object detection,” ser. Proceedings of the 31st ACM International Conference on Multimedia, 2023, pp. 7413–7423.
  - [43] S. Zhao, P. Cui, J. Shen, and H. Liu, “Local saliency consistency-based label inference for weakly supervised salient object detection using scribble annotations,” *CAAI Transactions on Intelligence Technology*, vol. 9, no. 1, pp. 239–249, 2024.
  - [44] B. Wan, X. Zhou, Y. Sun, T. Wang, S. Wang, H. Yin, C. Yan *et al.*, “Adnet: Anti-noise dual-branch network for road defect detection,” *Engineering Applications of Artificial Intelligence*, vol. 132, p. 107963, 2024.
  - [45] N. Yu, J. Wang, H. Shi, Z. Zhang, and Y. Han, “Degradation-removed multiscale fusion for low-light salient object detection,” *Pattern Recognition*, vol. 155, p. 110650, 2024.
  - [46] J. Yuan, X. Zou, H. Xia, T. Liu, and F. Wu, “Bi-branch multiscale feature joint network for orsi salient object detection in adverse weather conditions,” *IEEE Transactions on Geoscience and Remote Sensing*, 2024.
  - [47] Q. Chen, X. Yang, R. Lu, Q. Zhang, Y. Liu, X. Zhou, and B. Zheng, “Wxsod: A benchmark for robust salient object detection in adverse weather conditions,” *arXiv preprint arXiv:2508.12250*, 2025.
  - [48] Z. Chen, R. Cong, Q. Xu, and Q. Huang, “Dpanet: Depth potentiality-aware gated attention network for rgb-d salient object detection,” *IEEE Transactions on Image Processing*, vol. 30, pp. 7012–7024, 2020.
  - [49] H. Wen, C. Yan, X. Zhou, R. Cong, Y. Sun, B. Zheng, J. Zhang, Y. Bao, and G. Ding, “Dynamic selective network for rgb-d salient object detection,” *IEEE Transactions on Image Processing*, vol. 30, pp. 9179–9192, 2021.
  - [50] S. Yao, M. Zhang, Y. Piao, C. Qiu, and H. Lu, “Depth injection framework for rgb-d salient object detection,” *IEEE Transactions on Image Processing*, vol. 32, pp. 5340–5352, 2023.
  - [51] J. Li, W. Ji, M. Zhang, Y. Piao, H. Lu, and L. Cheng, “Delving into calibrated depth for accurate rgb-d salient object detection,” *International Journal of Computer Vision*, vol. 131, no. 4, pp. 855–876, 2023.
  - [52] R. Cong, H. Liu, C. Zhang, W. Zhang, F. Zheng, R. Song, and S. Kwong, “Point-aware interaction and cnn-induced refinement network for rgb-d salient object detection,” ser. Proceedings of the 31st ACM international conference on multimedia, 2023, pp. 406–416.
  - [53] W. Zhou, B. Wang, X. Dong, C. Xu, and F. Qiang, “Location, neighborhood, and semantic guidance network for rgb-d co-salient object detection,” *IEEE Transactions on Artificial Intelligence*, 2025.
  - [54] Y. Piao, Z. Rong, M. Zhang, W. Ren, and H. Lu, “A2dele: Adaptive and attentive depth distiller for efficient rgb-d salient object detection,” ser. Proceedings of the IEEE/CVF conference on computer vision and pattern recognition, 2020, pp. 9060–9069.
  - [55] N. Liu, N. Zhang, L. Shao, and J. Han, “Learning selective mutual attention and contrast for rgb-d saliency detection,” *IEEE Transactions*

- on *Pattern Analysis and Machine Intelligence*, vol. 44, no. 12, pp. 9026–9042, 2021.
- [56] Z. Tu, Z. Li, C. Li, and J. Tang, “Weakly alignment-free rgbt salient object detection with deep correlation network,” *IEEE Transactions on Image Processing*, vol. 31, pp. 3752–3764, 2022.
- [57] R. Cong, K. Zhang, C. Zhang, F. Zheng, Y. Zhao, Q. Huang, and S. Kwong, “Does thermal really always matter for rgb-t salient object detection?” *IEEE Transactions on Multimedia*, vol. 25, pp. 6971–6982, 2022.
- [58] H. Zhou, C. Tian, Z. Zhang, C. Li, Y. Ding, Y. Xie, and Z. Li, “Position-aware relation learning for rgb-thermal salient object detection,” *IEEE Transactions on Image Processing*, vol. 32, pp. 2593–2607, 2023.
- [59] H. Zhou, C. Tian, Z. Zhang, C. Li, Y. Xie, and Z. Li, “Frequency-aware feature aggregation network with dual-task consistency for rgb-t salient object detection,” *Pattern Recognition*, vol. 146, p. 110043, 2024.
- [60] H. Tang, Z. Li, D. Zhang, S. He, and J. Tang, “Divide-and-conquer: Confluent triple-flow network for rgb-t salient object detection,” *IEEE Transactions on Pattern Analysis and Machine Intelligence*, vol. 47, no. 3, pp. 1958–1974, 2025.
- [61] K. Wang, D. Lin, C. Li, Z. Tu, and B. Luo, “Alignment-free rgbt salient object detection: Semantics-guided asymmetric correlation network and a unified benchmark,” *IEEE Transactions on Multimedia*, vol. 26, pp. 10 692–10 707, 2024.
- [62] K. Wang, K. Chen, C. Li, Z. Tu, and B. Luo, “Alignment-free rgb-t salient object detection: A large-scale dataset and progressive correlation network,” ser. Proceedings of the AAAI Conference on Artificial Intelligence, 2025, pp. 7780–7788.
- [63] K. Song, J. Wang, Y. Bao, L. Huang, and Y. Yan, “A novel visible-depth-thermal image dataset of salient object detection for robotic visual perception,” *IEEE/ASME Transactions on Mechatronics*, vol. 28, no. 3, pp. 1558–1569, 2022.
- [64] L. Bao, X. Zhou, X. Lu, Y. Sun, H. Yin, Z. Hu, J. Zhang, and C. Yan, “Quality-aware selective fusion network for vdt salient object detection,” *IEEE Transactions on Image Processing*, vol. 33, pp. 3212–3226, 2024.
- [65] N. Huang, Y. Yang, R. Xi, Q. Zhang, J. Han, and J. Huang, “Salient object detection from arbitrary modalities,” *IEEE Transactions on Image Processing*, 2024.
- [66] N. Huang, Y. Yang, Q. Zhang, J. Han, and J. Huang, “Modality prompts for arbitrary modality salient object detection,” *arXiv preprint arXiv:2405.03351*, 2024.
- [67] K. Wang, Z. Tu, C. Li, Z. Liu, and B. Luo, “Unified-modal salient object detection via adaptive prompt learning,” *IEEE Transactions on Circuits and Systems for Video Technology*, 2025.
- [68] H. Gupta, O. Kotlyar, H. Andreasson, and A. J. Lilienthal, “Robust object detection in challenging weather conditions,” in *Proceedings of the IEEE/CVF Winter Conference on Applications of Computer Vision*, 2024, pp. 7523–7532.
- [69] K. Zhang, X. Yan, Y. Wang, and J. Qi, “Adaptive dehazing yolo for object detection,” in *International Conference on Artificial Neural Networks*. Springer, 2023, pp. 14–27.
- [70] H. Wu, Y. Qu, S. Lin, J. Zhou, R. Qiao, Z. Zhang, Y. Xie, and L. Ma, “Contrastive learning for compact single image dehazing,” in *Proceedings of the IEEE/CVF conference on computer vision and pattern recognition*, 2021, pp. 10 551–10 560.
- [71] C. Li, H. Zhou, Y. Liu, C. Yang, Y. Xie, Z. Li, and L. Zhu, “Detection-friendly dehazing: Object detection in real-world hazy scenes,” *IEEE Transactions on Pattern Analysis and Machine Intelligence*, vol. 45, no. 7, pp. 8284–8295, 2023.
- [72] H. Li, K. Yu, J. Qiu, Z. Wang, and Y. Yang, “Ia-det: Iterative attention-based robust object detection in adverse traffic scenes,” *IEEE Transactions on Instrumentation and Measurement*, 2024.
- [73] L. Wang, H. Qin, X. Zhou, X. Lu, and F. Zhang, “R-yolo: A robust object detector in adverse weather,” *IEEE Transactions on Instrumentation and Measurement*, vol. 72, pp. 1–11, 2022.
- [74] J. Wei, S. Wang, and Q. Huang, “F<sup>3</sup>net: fusion, feedback and focus for salient object detection,” ser. Proceedings of the AAAI conference on artificial intelligence, 2020, pp. 12 321–12 328.
- [75] H. Wang, Y. Zhao, F. Zhang, G. Gui, L. Yu, B. Chen, M. Liao, C. Yang, and W. Gui, “R-net: Recursive decoder with edge refinement network for salient object detection,” *Expert Systems with Applications*, vol. 261, p. 125562, 2025.
- [76] X. Zeng, M. Xu, Y. Hu, H. Tang, Y. Hu, and L. Nie, “Adaptive edge-aware semantic interaction network for salient object detection in optical remote sensing images,” *IEEE Transactions on Geoscience and Remote Sensing*, vol. 61, pp. 1–16, 2023.
- [77] Y. Gu, H. Xu, Y. Quan, W. Chen, and J. Zheng, “Orsi salient object detection via bidimensional attention and full-stage semantic guidance,” *IEEE Transactions on Geoscience and Remote Sensing*, vol. 61, pp. 1–13, 2023.
- [78] J. Zhu, X. Qin, and A. Elsaddik, “Dc-net: Divide-and-conquer for salient object detection,” *Pattern Recognition*, vol. 157, p. 110903, 2025.
- [79] Y.-H. Wu, Y. Liu, L. Zhang, M.-M. Cheng, and B. Ren, “Edn: Salient object detection via extremely-downsampled network,” *IEEE Transactions on Image Processing*, vol. 31, pp. 3125–3136, 2022.
- [80] D. Serrano-Lozano, L. Herranz, S. Su, and J. Vazquez-Corral, “Adaptive blind all-in-one image restoration,” *arXiv preprint arXiv:2411.18412*, 2024.
- [81] S. Rajagopalan, N. G. Nair, J. N. Paranjape, and V. M. Patel, “Gendeg: Diffusion-based degradation synthesis for generalizable all-in-one image restoration,” ser. Proceedings of the Computer Vision and Pattern Recognition Conference, 2025, pp. 28 144–28 154.
- [82] H. Gao, J. Yang, Y. Zhang, N. Wang, J. Yang, and D. Dang, “Prompt-based ingredient-oriented all-in-one image restoration,” *IEEE Transactions on Circuits and Systems for Video Technology*, vol. 34, no. 10, pp. 9458–9471, 2024.
- [83] G. Wu, J. Jiang, K. Jiang, X. Liu, and L. Nie, “Learning dynamic prompts for all-in-one image restoration,” *IEEE Transactions on Image Processing*, 2025.
- [84] P.-T. De Boer, D. P. Kroese, S. Mannor, and R. Y. Rubinstein, “A tutorial on the cross-entropy method,” *Annals of operations research*, vol. 134, no. 1, pp. 19–67, 2005.
- [85] Z. Wang, E. P. Simoncelli, and A. C. Bovik, “Multiscale structural similarity for image quality assessment,” ser. The thirty-seventh asilomar conference on signals, systems & computers, 2003, vol. 2. Ieee, 2003, pp. 1398–1402.
- [86] G. Mátyus, W. Luo, and R. Urtasun, “Deeproadmapper: Extracting road topology from aerial images,” ser. Proceedings of the IEEE international conference on computer vision, 2017, pp. 3438–3446.
- [87] W. Cui, K. Song, H. Feng, X. Jia, S. Liu, and Y. Yan, “Autocorrelation-aware aggregation network for salient object detection of strip steel surface defects,” *IEEE transactions on instrumentation and measurement*, vol. 72, pp. 1–12, 2023.
- [88] X. Lu, Y. Yuan, X. Liu, L. Wang, X. Zhou, and Y. Yang, “Low-light salient object detection by learning to highlight the foreground objects,” *IEEE Transactions on Circuits and Systems for Video Technology*, vol. 34, no. 8, pp. 7712–7724, 2024.
- [89] M. Zhuge, D.-P. Fan, N. Liu, D. Zhang, D. Xu, and L. Shao, “Salient object detection via integrity learning,” *IEEE Transactions on Pattern Analysis and Machine Intelligence*, vol. 45, no. 3, pp. 3738–3752, 2022.
- [90] Y. Liu, L. Zhou, G. Wu, S. Xu, and J. Han, “Tegnet: Type-correlation guidance for salient object detection,” *IEEE Transactions on Intelligent Transportation Systems*, vol. 25, no. 7, pp. 6633–6644, 2023.
- [91] F. Perazzi, P. Krähenbühl, Y. Pritch, and A. Hornung, “Saliency filters: Contrast based filtering for salient region detection,” ser. 2012 IEEE conference on computer vision and pattern recognition. IEEE, 2012, pp. 733–740.
- [92] D.-P. Fan, M.-M. Cheng, Y. Liu, T. Li, and A. Borji, “Structure-measure: A new way to evaluate foreground maps,” ser. Proceedings of the IEEE international conference on computer vision, 2017, pp. 4548–4557.
- [93] R. Achanta, S. Hemami, F. Estrada, and S. Susstrunk, “Frequency-tuned salient region detection,” ser. 2009 IEEE conference on computer vision and pattern recognition. IEEE, 2009, pp. 1597–1604.
- [94] D.-P. Fan, C. Gong, Y. Cao, B. Ren, M.-M. Cheng, and A. Borji, “Enhanced-alignment measure for binary foreground map evaluation,” *arXiv preprint arXiv:1805.10421*, 2018.
- [95] A. G. Howard, M. Zhu, B. Chen, D. Kalenichenko, W. Wang, T. Weyand, M. Andreetto, and H. Adam, “Mobilenets: Efficient convolutional neural networks for mobile vision applications,” *arXiv preprint arXiv:1704.04861*, 2017.
- [96] S. Mehta and M. Rastegari, “Mobilevit: light-weight, general-purpose, and mobile-friendly vision transformer,” *arXiv preprint arXiv:2110.02178*, 2021.